Funding proposal for the neutron decay spectrometer Nab at SNS

Precise Measurement of $\lambda = G_A/G_V$ and Search for Non-(V−A) Weak Interaction Terms in Neutron Decay

R. Alarcon[a], L.P. Alonzi[b], S. Baeßler[b,*], S. Balascuta[a], J.D. Bowman[c,†], M.A. Bychkov[b], J. Byrne[d], J.R. Calarco[e], T.V. Cianciolo[c], C. Crawford[f], E. Frlež[b], M.T. Gericke[g], F. Glück[h], G.L. Greene[i], R.K. Grzywacz[i], V. Gudkov[j], F.W. Hersman[e], A. Klein[k], M.C. Lehman[b], J. Martin[l], S.T. McGovern[b], S. Page[g], A. Palladino[b], S.I. Penttilä[c,‡], D. Počanić[b,†], K.P. Rykaczewski[c], W.S. Wilburn[k], A. Young[m] [**the Nab Collaboration**]

[a] *Department of Physics, Arizona State University, Tempe, AZ 85287-1504*
[b] *Department of Physics, University of Virginia, Charlottesville, VA 22904-4714*
[c] *Physics Division, Oak Ridge National Laboratory, Oak Ridge, TN 37831*
[d] *Department of Physics and Astronomy, University of Sussex, Brighton BN19RH, UK*
[e] *Department of Physics, University of New Hampshire, Durham, NH 03824*
[f] *Department of Physics and Astronomy, University of Kentucky, Lexington, KY 40506*
[g] *Department of Physics, University of Manitoba, Winnipeg, Manitoba, R3T 2N2 Canada*
[h] *IEKP, Universität Karlsruhe (TH), Kaiserstraße 12, 76131 Karlsruhe, Germany*
[i] *Department of Physics and Astronomy, University of Tennessee, Knoxville, TN 37996*
[j] *Department of Physics and Astronomy, Univ. of South Carolina, Columbia, SC 29208*
[k] *Los Alamos National Laboratory, Los Alamos, NM 87545*
[l] *Department of Physics, University of Winnipeg, Winnipeg, Manitoba R3B2E9, Canada*
[m] *Department of Physics, North Carolina State University, Raleigh, NC 27695-8202*

27 January 2010

Abstract: This document presents the motivation, experimental method, manpower and schedule for the Nab experiment at the Fundamental Neutron Physics Beamline at the SNS. Thanks to its highly precise theoretical treatment within the framework of the standard model and high sensitivity to departures from the basic $V-A$ description, neutron beta decay offers an attractive platform for searches for signals of new physics. The Nab experiment will precisely measure beta decays of the unpolarized neutron, with the goal to determine the electron–neutrino correlation with relative precision of 10^{-3}, and the Fierz interference term, a distortion of the beta spectrum never before measured in neutron decay, with an uncertainty of $\sim 3 \times 10^{-3}$. These results will lead to a new precise determination of the ratio $\lambda = G_A/G_V$ and to significant reductions in the allowed limits for both right- and left-handed scalar and tensor currents. Alternatively, the experiment will detect a nonzero signal consistent with certain realizations of supersymmetry. An optimized asymmetric magnetic and electrostatic spectrometer has been designed to achieve the required narrow momentum response function, and thus accomplish the physics goals of the experiment. Detailed breakdown of equipment cost, schedule of activities and distribution of collaborator effort are appended in separate spreadsheets.

*Experiment Manager
†Co-Spokesmen
‡On-site Manager

1. Physics motivation

Neutron β decay, $n \to pe\bar{\nu}_e$, is one of the basic processes in nuclear physics. Its experimental study provides the most sensitive means to evaluate the ratio of axial-vector to vector coupling constants $\lambda = G_A/G_V$. The precise value of λ is important in many applications of the theory of weak interactions, especially in astrophysics; e.g., a star's neutrino production is proportional to λ^2. More precise measurements of neutron β-decay parameters are also important in the search for new physics. Measurement of the neutron decay rate Γ, or lifetime $\tau_n = 1/\Gamma$, allows a determination of V_{ud}, the u-d Cabibbo-Kobayashi-Maskawa (CKM) matrix element, independent of nuclear models, because Γ is proportional to $|V_{ud}|^2$, as seen in the leading order expression:

$$\Gamma = \frac{1}{\tau_n} = \frac{f^R m_e^5 c^4}{2\pi^3 \hbar^7} \left(|G_V|^2 + 3|G_A|^2\right) \propto |G_V|^2 \left(1 + 3|\lambda|^2\right) = |V_{ud}|^2 \, |g_V|^2 \, G_F^2 (1 + 3|\lambda|^2)\,, \quad (1)$$

where $f^R = 1.71482(15)$ is a phase space factor, m_e is the electron mass, $g_{V,A}$ the vector and axial-vector weak nucleon form factors at zero momentum transfer, respectively, and G_F is the fundamental Fermi weak coupling constant. While the conservation of vector current (CVC) fixes g_V at unity, two unknowns, V_{ud} and λ, remain as variables in the above expression for Γ. Hence, an independent measurement of λ is necessary in order to determine V_{ud} from the neutron lifetime. Several neutron decay parameters can be used to measure λ; they are discussed below. Precise knowledge of V_{ud} helps greatly in establishing the extent to which the three-generation CKM matrix is unitary. CKM unitarity, in turn, provides an independent cross-check of the presence of certain processes and particles not included in the Standard Model (SM) of elementary particles and interactions, i.e., an independent constraint on new physics.

Currently, the most accurate value of the CKM matrix element V_{ud} is obtained from measurements of $0^+ \to 0^+$ nuclear β-decays, the so-called superallowed Fermi transitions [1]. However, the procedure of the extraction of V_{ud} involves calculations of radiative and nuclear structure corrections for the Fermi transition in nuclei. Despite the fact that these calculations have been done with high precision (see [2, 8] and references therein), it is impossible to verify the values of these nuclear corrections from independent experiments, and, as discussed below, questions concerning these corrections have been raised.

A problem with CKM matrix unitarity at the $2-3\sigma$ level persisted for over two decades. For example, the 2002 Review of Particle Properties [3] reported values of CKM matrix elements that yield for the first row

$$\Delta \equiv 1 - |V_{ud}|^2 - |V_{us}|^2 - |V_{ub}|^2 = (32 \pm 14) \times 10^{-4}\,. \quad (2)$$

The situation changed drastically in 2003 and 2004 when a series of experiments at Brookhaven, Fermilab and CERN reported revised values of K_{l3} decay branching ratios, leading to an upward adjustment, by about 2.5σ, of the CKM matrix element V_{us} [4, 5, 6]. Skipping the details of this revolutionary development, we note that a revised CKM unitarity check yields [7, 1]

$$\Delta = (1 \pm 10) \times 10^{-4}\,. \quad (3)$$

Thus, at least for a few years, the question of the CKM matrix unitarity appeared to be closed. However, a few questions related to V_{ud} still remain open. Several authors have recently questioned the Hardy and Towner analysis of superallowed Fermi $0^+ \to 0^+$ transitions [8], finding isospin-related corrections to be larger, thus leading to a smaller value for V_{ud}, and to possible CKM unitarity violation [9, 10, 11, 12]. This matter clearly remains to be definitively resolved.

Given the intrinsic theoretical complexity of nuclear beta decays, it is highly desirable to have an independent check of the superallowed Fermi nuclear beta decay result; neutron beta decay provides an excellent opportunity for that. Regrettably, a disturbing inconsistency persists between the best results on neutron decay and those on nuclear Fermi decays, as well as within the body of the neutron decay data.

Additionally, by its nature, neutron decay offers redundant consistency checks whose failure can be an indication of new physics.

We begin to discuss the last two points by briefly examining the neutron decay dynamics. Neglecting nucleon recoil, as well as radiative and loop corrections, the triple differential neutron decay rate is determined by the decay parameters a, b, A, B, etc., as shown:

$$\frac{dw}{dE_e d\Omega_e d\Omega_\nu} \propto p_e E_e (E_0 - E_e)^2 \left[1 + a\frac{\vec{p}_e \cdot \vec{p}_\nu}{E_e E_\nu} + b\frac{m_e}{E_e} + \langle \vec{\sigma}_n \rangle \cdot \left(A\frac{\vec{p}_e}{E_e} + B\frac{\vec{p}_\nu}{E_\nu} + \ldots \right) \right], \quad (4)$$

where $p_{e(\nu)}$ and $E_{e(\nu)}$ are the electron (neutrino) momenta and energies, respectively, E_0 is the electron energy spectrum endpoint, and $\vec{\sigma}_n$ is the neutron spin. The "lower-case" parameters: a, the electron–neutrino correlation, and b, the Fierz interference term, are measurable in decays of unpolarized neutrons, while the "uppercase" parameters, A and B, require polarized neutrons. All except b depend on the ratio $\lambda = g_A/g_V$, in the following way (given here at the tree level, with λ real):

$$a = \frac{1 - |\lambda|^2}{1 + 3|\lambda|^2}, \qquad A = -2\frac{|\lambda|^2 + \lambda}{1 + 3|\lambda|^2}, \qquad B = 2\frac{|\lambda|^2 - \lambda}{1 + 3|\lambda|^2}. \quad (5)$$

Given that $\lambda \simeq -1.27$, parameters A and a are similarly sensitive to λ:

$$\frac{\partial a}{\partial \lambda} = \frac{-8\lambda}{(1 + 3\lambda^2)^2} \simeq 0.30, \qquad \frac{\partial A}{\partial \lambda} = 2\frac{(\lambda - 1)(3\lambda + 1)}{(1 + 3\lambda^2)^2} \simeq 0.37, \quad (6)$$

while B is relatively insensitive:

$$\frac{\partial B}{\partial \lambda} = 2\frac{(\lambda + 1)(3\lambda - 1)}{(1 + 3\lambda^2)^2} \simeq 0.076. \quad (7)$$

Experimental status of the above parameters is summarized in the Particle Data Group's review in Ref. [1]. For some time, the best precision by far in extracting λ has been achieved through measurement of A, the correlation between the electron momentum and neutron spin. However, the experimental status of A and λ is far from satisfactory, as seen below.

Two beta asymmetry experiments finished their analysis recently, since the PDG 2008 compilation. The UCNA collaboration published $A = -0.1138(46)(21)$ [13]. The result of the last PERKEO II run, $A = -0.1198(5)$, will be published soon [14]. If we include these

new results along with those from previous experiments in a new average, as done by PDG [1], we obtain $\chi^2 = 28$ for 5 degrees of freedom, which is even less satisfactory than the previously reported PDG result (see Fig. 1). This disagreement carries over directly to the value of λ and, hence, to V_{ud}. One of the principal goals of the proposed Nab experiment is an independent determination of λ from a, the neutrino electron correlation coefficient. Such an evaluation will have entirely different systematic errors and might be even more precise.

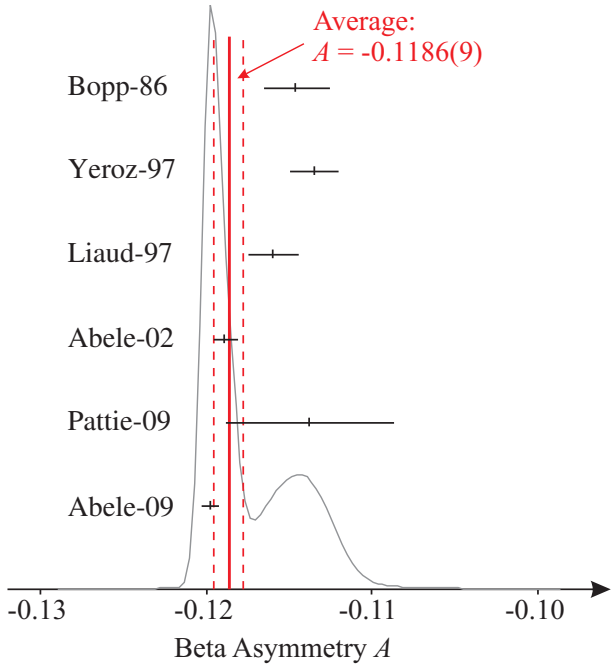

Figure 1: Updated compilation of the most precise measurements of the neutron beta asymmetry A; data are from Pattie et al. (2009) [13], Abele (2009) [14], Abele et al. (2002) [15], Liaud et al. (1997) [16], Yerozolimsky et al. (1997) [17], and Bopp et al. (1986) [18]. The average, $A = -0.1186(9)$, includes a scale factor of 2.3, as we obtain $\chi^2 = 28$ for 5 degrees of freedom. The statistical probability for such a high χ^2 is 5×10^{-5}.

We also note that recent studies of $T = \frac{1}{2}$ nuclear mirror transitions [19] have reached the precision of V_{ud} determination achieved thus far with neutron beta decays, i.e., through measurements of A, the beta asymmetry, and τ_n, neutron lifetime, as discussed above.

Just as interesting as the determination of $\lambda = G_A/G_V$ are the limits on non-SM interactions that can be extracted from studies of neutron beta decay. Multiple measurements of neutron decay correlation coefficients and the neutron lifetime on the one hand, and the well known lifetime of superallowed decays have been used to search for physics beyond the standard model. In the low energy limit, semileptonic decays can be universally described by a point-like interaction between currents of different type (vector, axial-vector, scalar, and tensor), and of different handedness.

$$H_{\rm if} = \frac{2G_{\rm F}V_{\rm ud}}{\sqrt{2}} \sum_{j\in\{\rm V,A,S,T\}} L_j \left\langle p\right| \Gamma_j \left|n\right\rangle \left\langle e^-\right| \Gamma_j \frac{1-\gamma_5}{2} \left|\nu_e\right\rangle + R_j \left\langle p\right| \Gamma_j \left|n\right\rangle \left\langle e^-\right| \Gamma_j \frac{1+\gamma_5}{2} \left|\nu_e\right\rangle \ . \tag{8}$$

The types of currents are defined by the operators

$$\Gamma_{\rm V} = \gamma_\mu \ ; \ \Gamma_{\rm A} = i\gamma_\mu\gamma_5 \ ; \ \Gamma_{\rm S} = 1 \ ; \ \Gamma_{\rm T} = \frac{i\left[\gamma_\mu,\gamma_\nu\right]}{2\sqrt{2}} \ . \tag{9}$$

The coupling constants leading to a left-handed neutrino and a right handed neutrino are denoted L_j and R_j, respectively. This parametrization was introduced by Glück et al.

[20]; these coupling constants are linear combinations of C_j and C'_j, the familiar couplings originally introduced in the 1950's [21, 22]:

$$C_j = \frac{G_F V_{ud}}{\sqrt{2}} (L_j + R_j)\,,\; C'_j = \frac{G_F V_{ud}}{\sqrt{2}} (L_j - R_j) \;\text{ for } j = \mathrm{V, A, S, T}\,. \tag{10}$$

In the standard model, the only nonvanishing coupling constants are $L_V = 1$ (CVC) and $L_A = \lambda$. In more general models, other coupling constants appear and certain measurement observables are modified. Details are given in Refs. [20, 21, 22].

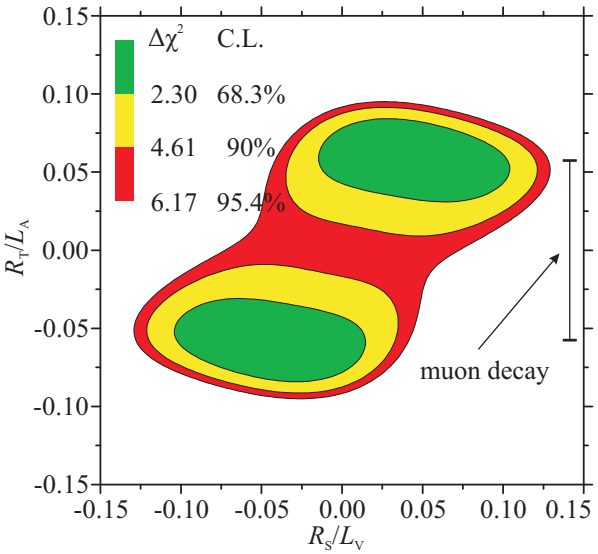

Figure 2: Present limits for right-handed scalar and tensor currents from neutron decay. The standard model prediction is at the origin of the plot. Analogous tensor limits extracted from muon decays are indicated as well—the scalar limits are larger than the scale of the plot (see text for details).

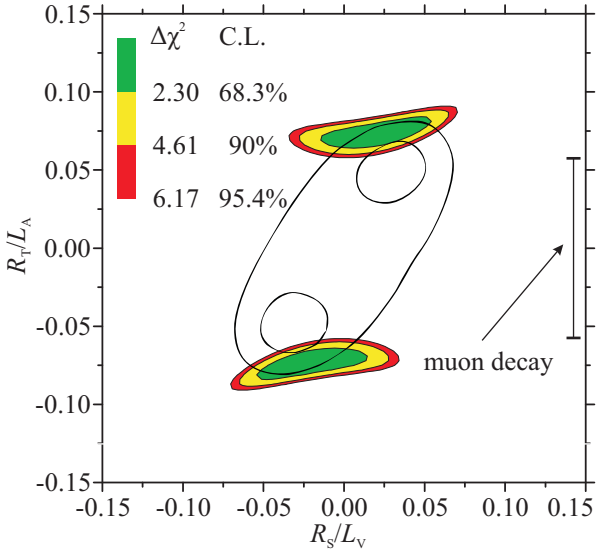

Figure 3: Future limits for right-handed scalar and tensor currents from neutron decay. The black lines are present 68.3% and 95.4% contours found in a recent survey of nuclear and neutron beta decays [23]. Analogous tensor limits extracted from muon decays (see text for details) are also indicated—the scalar limits are larger than the scale of the plot.

We first consider the Nab sensitivity to right-handed scalar and tensor currents. Fig. 2 shows the present limits from neutron decay. For neutron lifetime we used the value $\tau_n = 881.9(14)\,\mathrm{s}$ ([1] and [24]), $Ft = 3071.81\,\mathrm{s}$ from superallowed beta decays [8], the beta asymmetry $A = -0.1186(9)$ (our new average), the neutrino asymmetry $B = 0.9807(30)$ [1], and the neutrino electron correlation coefficient $a = -0.1030(40)$ [1] as input parameters for our study. Fig. 3 shows the improvement arising from an additional Nab measurement of $a = -0.1030(1)$ (reflecting the current world average for a and the projected Nab uncertainty). The black lines stem from a recent survey of the state of the art in nuclear and neutron beta decays [23]. The figure clearly demonstrates that the proposed Nab measurement of a in neutron decay is competitive. We note that Fig. 3 changes substantially if we

assume different measurement central value results for a. In this standard model extension, as well as in the SM itself, the Fierz interference term b has to be zero.

For completeness, we also consider the limits on non-(V−A) interaction couplings extracted from muon decay measurements [25, 1]. These limits relate to operators that are different from the ones encountered in neutron beta decays. However, in certain supersymmetric extensions of the standard model, the muon and neutron decay derived limits become comparable [26, 27]. For this reason we have included the corresponding limits from muon decays in Figs. 2 – 5, as appropriate.

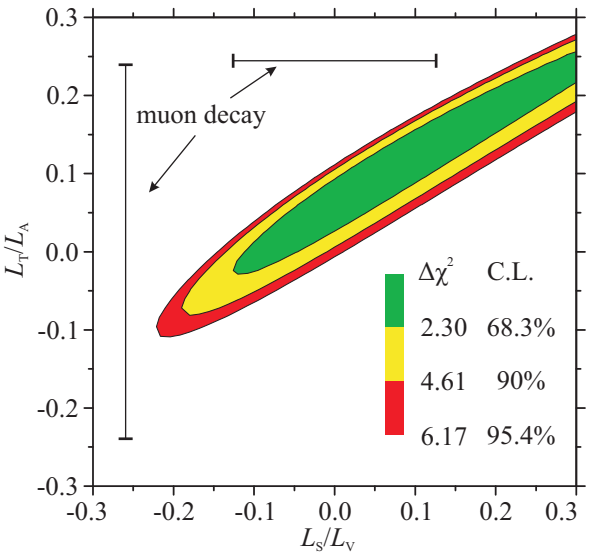

Figure 4: Present limits for left-handed scalar and tensor currents from neutron decay. The standard model prediction is at the origin of the plot. Analogous limits extracted from muon decays (see text for details) are also indicated.

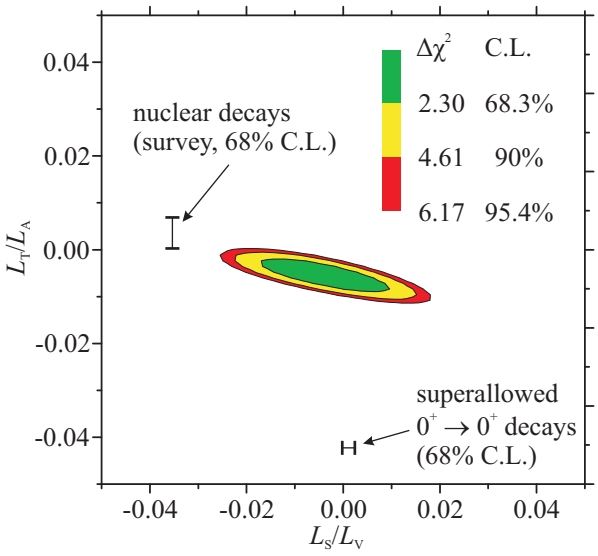

Figure 5: Future limits for left-handed scalar and tensor currents from neutron decay, assuming Nab measurements of $a = -0.1030(1)$ for the neutrino correlation coefficient, and $b = 0 \pm 0.003$ for the Fierz term, and including the present world average of τ_n, the neutron lifetime (bound to improve by the time Nab is completed). Analogous limits extracted from muon decays (see text for details) are not indicated since they exceed the scale of the plot.

We next turn to a model with left-handed scalar and tensor currents. In this model, a non-vanishing Fierz term b appears, and its measurement is the most sensitive way to constrain the size of the non-standard currents. Fig. 4 shows the current limits from neutron decay. Compared to the input data for Fig. 2, we leave out the lifetime, since the Ft value used is obtained assuming a vanishing Fierz term. Fig. 5 demonstrates the impact of the projected Nab measurements of the neutrino–electron correlation coefficient a and the Fierz interference term b. For comparison, a recent combined analysis of neutron and nuclear physics data (see Ref. [23]) finds $L_S/L_V = 0.0013(13)$ and $L_T/L_A = 0.0036(33)$. New neutron data, in combination with the updated limit on L_S from superallowed beta decays

[8], would improve the limit on $L_{\rm T}$ slightly. In addition, supersymmetric contributions to the standard model can be discovered at this level of precision, as discussed in [26].

As a final note, we comment on comparisons with similar limits extracted from pion decays. The presence of a tensor interaction would manifest itself in both the Fierz interference term in beta decays (e.g., of the neutron) and in a non-zero value of the tensor form factor for the pion. The latter was hinted at for well over a decade, but was recently found to be constrained to $-5.2\times10^{-4} < F_T < 4.0\times10^{-4}$ with 90% confidence [28]. While values for b in neutron decay and for the pion F_T are not directly comparable, in certain simple scenarios they would be of the same order [29]. Thus, finding a nonzero value for b in neutron decay at the level of $\mathcal{O}(10^{-3})$ would be extremely interesting. Similarly, the $\pi \to e\nu$ decay (π_{e2}) offers a very sensitive means to study non-(V−A) weak couplings, primarily through a pseudoscalar term in the amplitude. (Alternatively, π_{e2} decay provides the most sensitive test of lepton universality.) Thus, the measurements proposed here will complement the results of precision experiments in the pion sector, such as PIBETA [30], PEN [31], PiENu [32].

2. Design of the asymmetric spectrometer

Our method to determine the electron–neutrino correlation a, one of the two target observables in the Nab experiment, requires the detection of both the proton and electron in neutron decay, and the determination of their energies or momenta. This basic principle is illustrated in Fig. 6 which plots the available phase space in the $p_{\rm p}^2$-$E_{\rm e}$ plane. The plot shows that a is determined by measuring the slope of the $p_{\rm p}^2$ probability distribution for fixed $E_{\rm e}$. While the Fierz interference term could in principle be determined from a precise measurement of the beta energy spectrum alone, coincident detection of the accompanying proton is essential in suppressing the singles background.

The basic idea of the proton time of flight (TOF) spectrometer was introduced in the Nab proposal [33] and subsequently published in Ref. [34]. Neutrons decay in a magnetic field that guides the electrons and protons to large-area segmented Si detectors. After a rapid field expansion region, the magnetic field is weak for most of the flight path, and the proton and electron momenta are nearly parallel to the field. Hence, the measured proton time of flight yields the proton energy. The pulse height in the Si detectors gives the electron energy. The angle between the electron and neutrino is inferred from the proton energy distribution for each electron energy.

We determine the neutrino electron correlation coefficient for each electron energy $E_{\rm e}$ with a fit to the measured $1/t_{\rm p}^2$ spectrum, given as

$$P_t(1/t_{\rm p}^2) = \int P_p(p_{\rm p}^2)\Phi(1/t_{\rm p}^2, p_{\rm p}^2)dp_{\rm p}^2\,. \tag{11}$$

where $\Phi(1/t_{\rm p}^2, p_{\rm p}^2)$ is the detection function, which describes the averaging over the relevant unobserved quantities. These are θ_0, the angle between proton momentum and magnetic field at the moment of the decay, and the position of the neutron decay. Since the detection function is small, a measurement of $1/t_{\rm p}^2$ is approximately equivalent to a measurement of the squared proton momentum $p_{\rm p}^2$. The shape of the distribution $P_p(p_{\rm p}^2)$ of the proton momentum squared (i.e., the proton energy) for a given electron energy $E_{\rm e}$, reflects the value of a, the

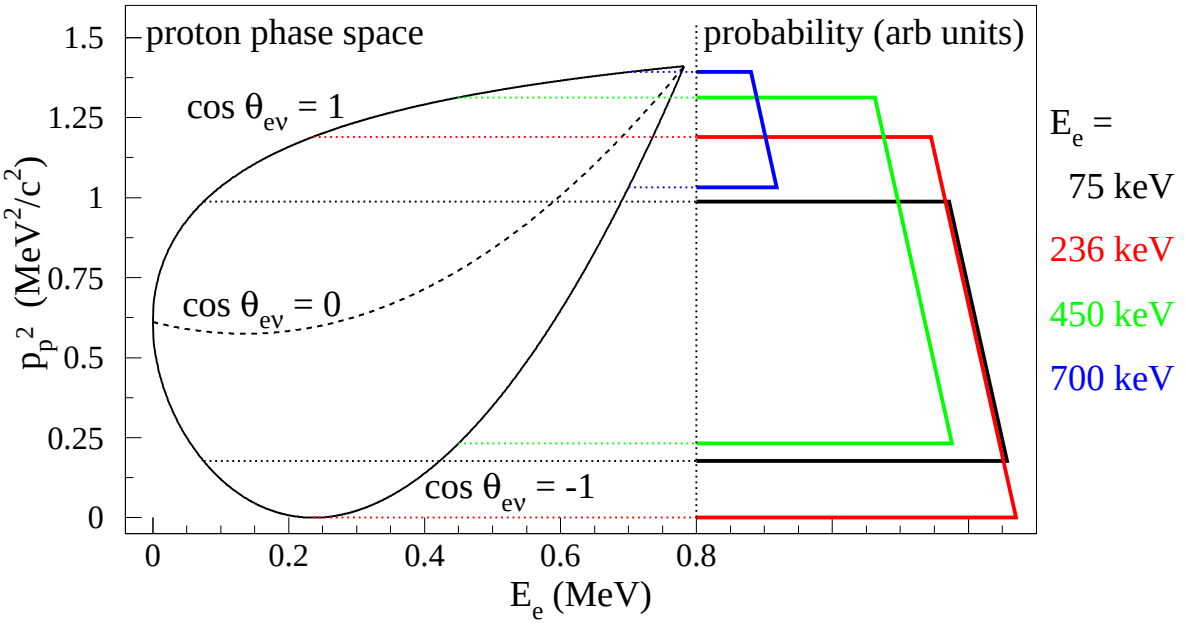

Figure 6: Allowed phase space for electron (E_e) and proton energy ($\propto p_\mathrm{p}^2$). At the upper (lower) limit of the proton energy spectrum for a fixed E_e, the electron and neutrino momenta are parallel (antiparallel). If the electron–neutrino correlation $a = 0$, the probability distribution of p_p^2 for a given electron energy E_e would be uniform, i.e., a rectangular box spectrum. The realistic projected probability distributions are shown in the right panel of the figure for $a = -0.103$, the current central value, for four electron energies, as indicated.

neutrino–electron correlation coefficient. The quantity $\cos\theta_{e\nu}$ can be expressed as a function of p_p, the proton momentum, and E_e, the electron energy, which fixes p_e and p_ν, through

$$p_\mathrm{p}^2 = p_\mathrm{e}^2 + 2p_\mathrm{e}p_\nu \cos\theta_{\mathrm{e}\nu} + p_\nu^2 \,. \tag{12}$$

Thus, using $\beta = v_\mathrm{e}/c$, $P_p(p_\mathrm{p}^2)$ is given by:

$$P_p(p_\mathrm{p}^2) = \begin{cases} 1 + a\beta\frac{p_\mathrm{p}^2 - p_\mathrm{e}^2 - p_\nu^2}{2p_\mathrm{e}p_\nu} & \text{for } \left|\frac{p_\mathrm{p}^2 - p_\mathrm{e}^2 - p_\nu^2}{2p_\mathrm{e}p_\nu}\right| < 1 \,, \\ 0 & \text{otherwise.} \end{cases} \tag{13}$$

The Si detectors accurately measure the electron energy with keV-level resolution. No electron energy is lost through backscattering of electrons because the magnetic guide field causes every electron to be absorbed in one or the other Si detector, regardless of which detector is impacted first. Only small corrections for backscattering and for bremsstrahlung have to be made.

The measurement of the proton energy is less accurate because the proton momentum requires a certain minimum distance to be longitudinalized. Compared to the symmetric spectrometer design presented in the original Nab proposal [33], the asymmetric configuration significantly narrows the response function while maintaining a workable count rate. The width of the proton energy resolution function is about 3–4% in the asymmetric configuration, which, through energy smearing, leads to a small but significant correlation between

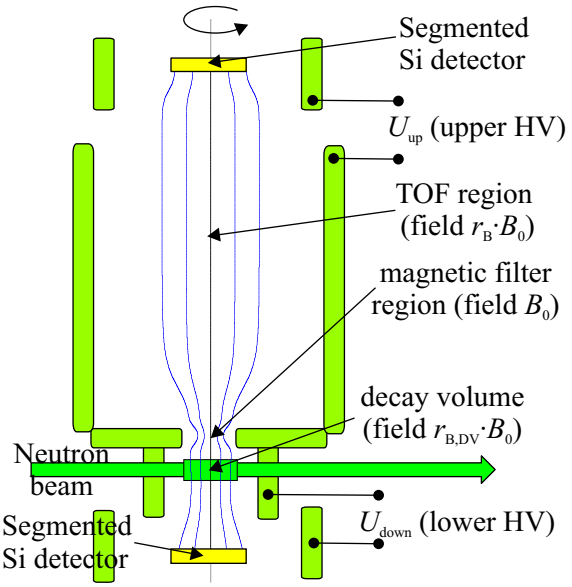

Figure 7: Sketch of the setup of an asymmetric Nab, not to scale. The electric and magnetic fields (electrodes, in light green, and coils, not shown) have cylindrical symmetry around the vertical axis.

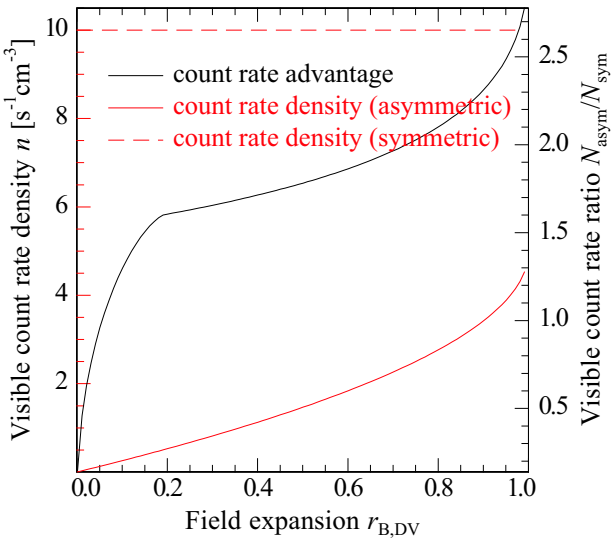

Figure 8: Statistical Sensitivity: The red lines show the proton count rate normalized to the decay volume size in symmetric (solid red line) and asymmetric (dashed red line) configuration. The black solid line is drawn towards the right axis and shows the ratio of visible count rates.

the value of a and the proton time of flight response function. Making the response function narrow decreases the fraction of the proton energy spectrum that is smeared out and reduces the correlation between the shape of the response function and a. In the original symmetric configuration, the neutrons decayed in the region with the maximum magnetic field. The requirements of a large decay volume and a narrow response function were in sharp conflict. The asymmetric configuration is shown conceptually in Fig. 7. Here, the neutrons decay in a region of moderate magnetic field, and the decay protons have to pass through a field pinch (the filter region) above the decay volume to be detected in the upper detector, the only detector that detects protons. In contrast to the symmetric configuration, where every decay proton, irrespective of its initial direction, is accepted, only upward-going decay protons are accepted in the asymmetric configuration. In the symmetric configuration, the flight path was limited by the depth of the pit below the spectrometer. In the asymmetric configuration, the lower flight path is not used for the TOF measurement, and can be relatively short, while the upper flight path, which is used to measure the proton TOF, can be long, leading to a narrower response function. Finally, the source height contributes to the width of the resolution function for both the symmetric and asymmetric configurations, but to a lesser extent in the asymmetric configuration, because the range of accepted proton directions with respect to the magnetic guide field is much narrower. The ability to accept a larger decay volume mitigates the loss of protons at large decay angles.

The width of the response function is given by the sharpness of the magnetic field pinch

and the dispersion in the time spent between the decay region and the approach to the field maximum. The time resolution, dominated by the magnetic field properties in the decay and filter regions, is better for the asymmetric than the symmetric design. This advantage is further enhanced by an extended low magnetic field region above the filter which allows for a long average proton time of flight, giving the response function a much more favorable relative width than is possible in the symmetric confirguration. Finally, the neutron beam is kept at a higher magnetic field than the detectors, to longitudinalize the electron momenta.

Compared to the symmetric one, the asymmetric configuration leads to a loss of many decay events, as only a small $\cos\theta_0$ range is accepted. In the adiabatic approximation the upper detector accepts all protons with $\cos\theta_0 \in (\cos\theta_{\rm min}, 1)$, where

$$\cos\theta_{\rm min} = \sqrt{1 - r_{\rm B,DV}}\,, \tag{14}$$

and $r_{\rm B,DV}$ is the ratio between the magnetic field in decay volume and filter region. This loss is compensated by the bigger decay volume. In the symmetric configuration, the decay volume is restricted by the need to have the central coil pair close together for a sharp decay field profile. Figure 8 shows the comparison for different magnetic field ratios $r_{\rm B,DV}$. While the count rate of the detected protons (the "visible" count rate) per unit decay volume is strongly reduced, the total amount of detected protons stays about the same for moderate field expansion ratios of $r_{\rm B,DV} = 0.4$ thanks to greatly larger decay volume. Since the same number of protons are detected in the asymmetric and in the symmetric configuration, the statistical sensitivities of the two are equal. The simulation in Fig. 8 assumes a size of the decay volume in the symmetric configuration of $V_{\rm sym} = 20\,{\rm cm}^3$ [33], a neutron decay density in the decay volume of $n = 10\,{\rm s}^{-1}{\rm cm}^{-3}$, and an accepted neutron beam height of 8 cm in the asymmetric configuration. We have conservatively reduced the value of $n = 19.5\,{\rm s}^{-1}{\rm cm}^{-3}$ given in [35] to take into account likely beam losses due to windows and collimation. The radial size of the decay volume is limited by the condition that the protons have to pass the electrode in the filter region, which is assumed to have a minimum radius of 2.2 cm. This setup is discussed below.

The main advantage of the asymmetric configuration is the systematics:

a. **Detection function:** The relative width of the response function, given in terms of the detection function $\Phi(1/t_{\rm p}^2, p_{\rm p}^2)$ in [33], is considerably smaller for the asymmetric configuration. The bigger flightpath length and the sharper magnetic field pinch outweigh the fact that the protons have to pass the increasing and decreasing side of the field pinch. In the original proposal we discussed two methods to determine the detection function. In method A we determine the whole shape of the detection function based on the edges of the measured $1/t_{\rm p}^2$ spectrum for a given fixed electron energy. In method B we determine the detection function from the geometry and the electromagnetic field configuration, with the exception of the spectrometer length and the electron energy calibration, which remain free parameters. Both methods become more precise as the detection function is made narrower. We plan two additional tests: (i) we will vary the magnetic field ratio between the filter and the decay volume, and (ii) we will measure with different heights of the collimated neutron beam. The agreement of the extracted values for a for configurations with different detection functions is an important additional crosscheck of our systematics.

b. **Sensitivity to small field inhomogeneities:** The symmetric configuration imposed very tight constraints on local magnetic or electric field minima in the decay region. The resulting tolerance on the value of the electric potential in the symmetric configuration was several μV. Separating the decay volume and the filter (peak magnetic field) region provides an advantage: the only region where particles could be trapped due to electric and magnetic field inhomogeneities is in the decay volume. Protons which are trapped there can be neglected, as they would not be able to pass the filter region anyway. (Too many trapped protons could, however, exacerbate a background problem, discussed below.) Electrical potential and magnetic field inhomogeneities influence $t_{\rm p}$, the proton TOF, in the asymmetric configuration as well; however, inhomogeneities at the level of about 10 mV level can be tolerated.

c. **In situ determination of the detector solid angle:** Another feature of the asymmetric setup is that the average of $\cos\theta_0$ for the protons, as well as for the electrons, can be determined experimentally. For Nab this means that $\cos\theta_{\rm min}$ and $r_{\rm B,DV}$ can be determined in situ (for details see App. D, 2$^{\rm nd}$ part). Furthermore, this determination allows the asymmetric spectrometer to be used to measure the beta asymmetry A and the proton asymmetry C, from which the neutrino asymmetry B can be evaluated. The systematic uncertainties are smaller than for the symmetric configuration, while the statistical uncertainties are comparable. These asymmetry measurements are discussed further in Sec. 7.

d. **Electric potential distribution and particle trapping:** In the symmetric configuration, the magnetic field in combination with the electric potential distribution forms a Penning trap for negatively charged particles. Low energy decay electrons, as well as electrons from residual gas ionization through radiation, are trapped permanently and will ionize the residual gas. Positive ions from these ionization processes will be accelerated toward one of the detectors and cause an uncorrelated background. In addition, high voltage breakdown due to Penning discharges presents a danger. While it might be possible to deal with this background through electrode design, good vacuum, or via the removal of trapped particles by means of electric fields or mechanically, a better approach is to avoid the Penning trap altogether. In the asymmetric configuration, we will run the upper detector at -30 kV, and the remainder of the spectrometer at ground potential (see Fig. 7). In this way, the main Penning trap is removed, and in addition, the field emission currents from the different electrodes due to the high voltage are reduced compared to the original design. However, careful electrode design is still needed to avoid HV instabilities and background production due to smaller traps, e.g., between electrode and cryostat surfaces (observed in [36]).

In the measurement of b, the Fierz interference term, the proposed asymmetric spectrometer configuration selects only events with protons moving in a limited range of directions. An angular dependence in our detector response function for electrons, e.g., due to electron backscattering, would present the difficult task of disentangling the angular dependence of the electron spectrum of those electrons whose associated protons are detected in the upper detector. However, we have the option to run the spectrometer in a different configuration

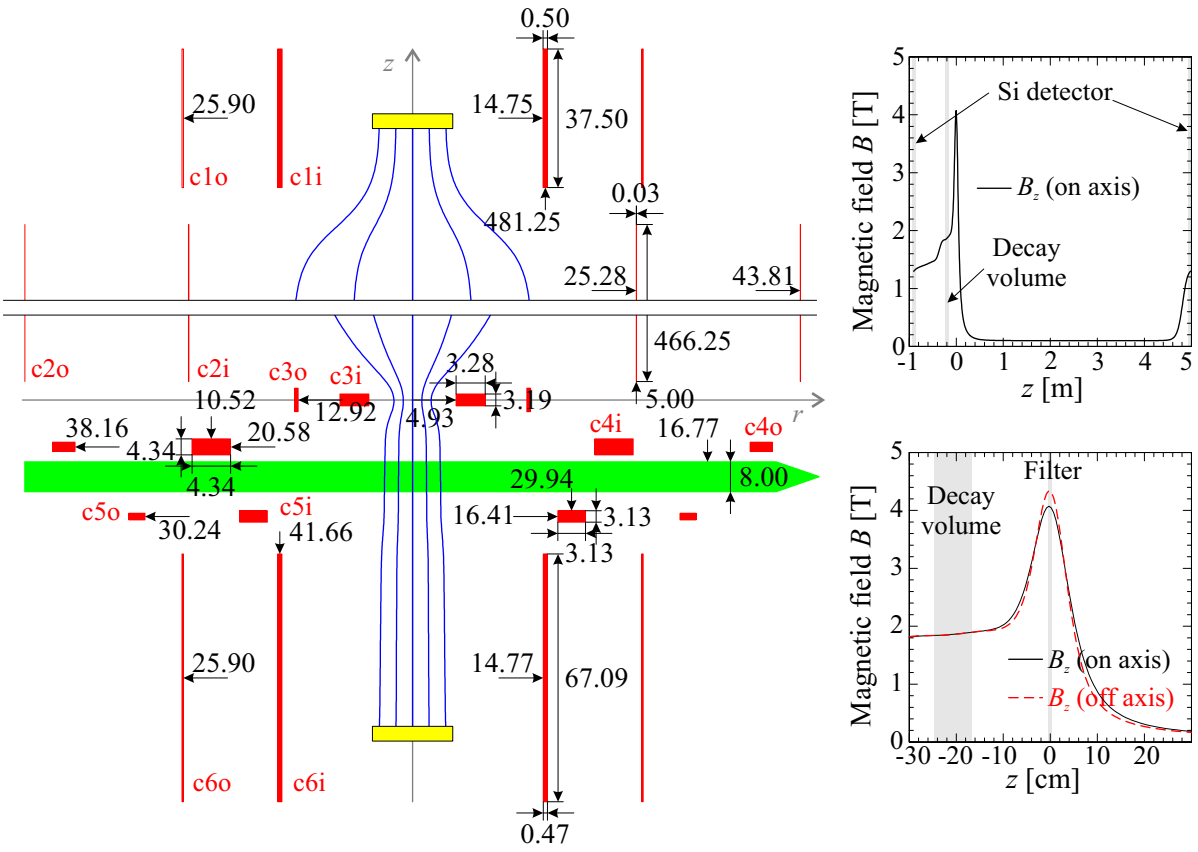

Figure 9: Coil design: The system is cylindrically symmetric around the vertical (z) axis. Vertical distances are given relative to the axis of the coordinate system. All dimensions are given in cm. Coils are drawn in red. The shaded thick green arrow depicts the neutron beam. Magnetic field lines are shown in blue, and the detectors are shown in yellow. We note that about 4 m of space is omitted in the center of the coil pair c2i/c2o. The diagrams on the right-hand side depict the magnetic field profiles.

with the lower detector at −30 kV, and the remainder of the spectrometer at ground potential (see Fig. 7), plus a mirror voltage of +1 kV in the filter region. In this configuration we would detect all protons in the lower detector, and the measured electron energy distribution would not depend on the electron impact angle onto the detector.

A possible superconducting magnet coil system is shown in Fig. 9. The coil system has cylindrical symmetry around the vertical symmetry axis. The system is actively shielded to comply with the SNS policy about stray magnetic fields: each outer coil has a current orientation opposite to the inner coil. In addition, there will be a passive antimagnetic screen made of steel (not shown in the drawing), similar to the one described in Ref. [37].

The decay volume is a cylinder of radius 3.13 cm, height 8 cm, and volume of 246 cm^3. The expected neutron decay rate is about 2,500 s^{-1}, out of which 13% of the protons are detected in the upper detector. GEANT4 simulations demonstrated that the detection function in this configuration has a relative width (defined as RMS/mean) of 3.8% (see Fig. 10). The simulation depicted in this figure neglects small corrections due to the acceleration field, and

the electron TOF.

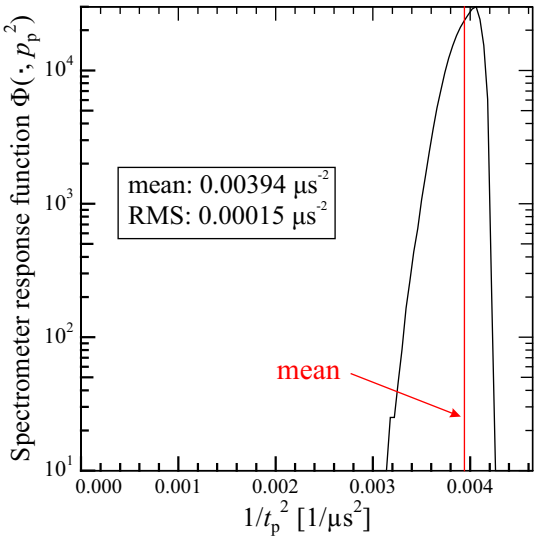

Figure 10: Detection function: Detector response for a proton with momentum $p_p^2 = 0.95\,\mathrm{MeV/c}$.

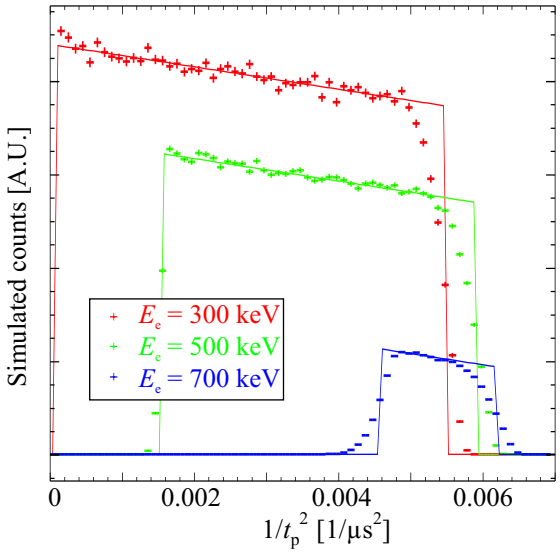

Figure 11: Proton $1/t_\mathrm{p}^2$ spectrum for different values of fixed electron energy E_e. The solid line is the expectation for an infinitely sharp detection function.

Figure 11 shows the proton $1/t_\mathrm{p}^2$ spectrum for different electron energies E_e. The data points are the results of a GEANT4 simulation. The solid lines show the expectation for a detection function which is infinitely sharp. For a perfect detector, the $1/t_\mathrm{p}^2$ spectrum would have a slope proportional to a, the neutrino–electron correlation coefficient, within the range of $1/t_\mathrm{p}^2$ allowed by the decay kinematics, and would drop sharply to zero outside (see Eqs. (11) and (13) and the original Nab proposal [33]). The main effect of the detection function is to soften these edges. The measured data at the edges can be used to determine the detection function experimentally.

We now turn to the relationship between t_p, the proton TOF, and p_p, the proton momentum, in order to determine $\Phi(1/t_\mathrm{p}^2, p_\mathrm{p}^2)$, the detection function. In the adiabatic approximation t_p is given by [33, 38]:

$$t_\mathrm{p} = \frac{m_\mathrm{p}}{p_\mathrm{p}} \int \frac{dz}{\sqrt{1 - \frac{B(z)}{B_0}\sin^2\theta_0 - \frac{e(U(z)-U_0)}{T_0}}}\,, \tag{15}$$

where m_p is the proton mass, while B_0 and U_0 are the magnetic field and electric potential, respectively, at the point of decay. The initial values are taken for p_p and T_0, the proton momentum and energy, respectively. The proton gyrates around a magnetic field line, and the integral is taken along this field line from its initial value at the decay point all the way to the detector. Imperfect knowledge of the detection function, is the principal source of systematic uncertainties. The main contribution to the width of $\Phi(1/t_\mathrm{p}^2, p_\mathrm{p}^2)$ (see Fig. 10) comes from the different times of flight to the detector for protons with equal energy but different emission angle θ_0 relative to the magnetic field. The most important property of

the spectrometer influencing the spread in the proton TOF for a given p_p is the magnetic field in the filter region. Our optimization resulted in a compromise between a very high field curvature in the filter region (that is, a small detection function) and a reasonably big decay volume (that is: a coil c3i that is not too small).

3. The Si detectors

Detector choice and design is a challenging issue for any precise neutron beta decay experiment. The detector has to be able to stop and detect the full energy of 50–750 keV electrons as well as 30 keV protons. This requires a detector thickness of about 2 mm Si-equivalent, a very thin window technology, and a very low energy threshold for detecting signals down to about 10 keV.

The very thin window/dead-layer should uniformly cover a large area of $\simeq$100 cm^2. The detector has to be segmented into about 100 elements. The segmentation has to be applied on the back side to keep the irradiated front side homogeneous. The segmentation is necessary to determine the particle position and thus to identify the electron/proton trajectory. The time and spatial pattern of electron energy deposition has to be measured. The detector segmentation has to be combined with pulse processing electronics allowing for real-time signal recording with a resolution at the level of several ns. The low energy threshold is related to good energy resolution, at the level of a few keV for the relevant energy range of electrons and protons.

A cooled silicon detector has the optimal combination of efficiency, stability, energy resolution and timing resolution unsurpassed by other types of detector, some of which may excel in one of the above characteristics, but not in all.

The design goal, pursued in a collaboration with Micron Semiconductor Ltd., has been to build a large area segmented single wafer silicon detector, about 2 mm thick to enable stopping the electrons, and operating with a liquid nitrogen cooling at the temperature level of about 100 K. The readout will be implemented using cold-FET preamplifier and real-time digital signal processing electronics. Charged particles will enter the detector through the junction side, which is uniform, apart from a very thin aluminum grid deposited on it with a coverage of 0.4%. Charge liberated by the ionizing particles will be collected on the ohmic side. The active area of the detector will be segmented into 127 individual elements. A sketch of the design of the segmented ohmic side of the detector is shown in Fig. 12.

A hexagonal array of detector elements is chosen for several reasons.

1. Hexagons efficiently fill the circular area of the detector,
2. they match the image of the decay volume well,
3. only three detector elements meet at a vertex, reducing the number of elements involved in a charge-sharing event, and
4. the number of adjacent elements that must be searched for the partner particle or reflected electron events is minimized.

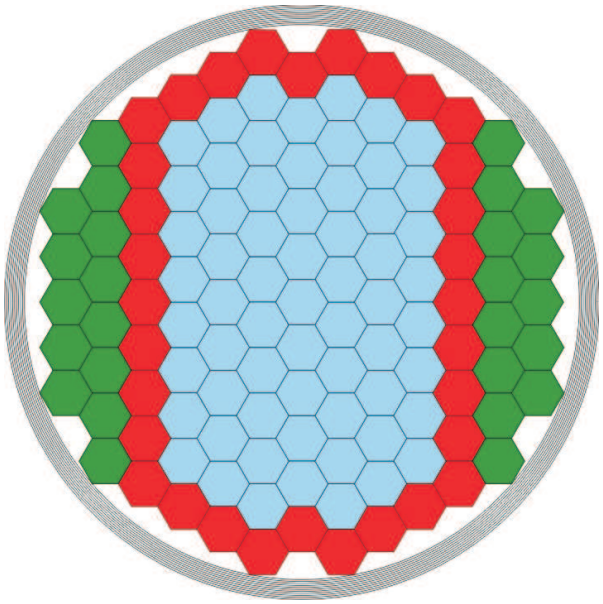

Figure 12: Above: design of the ohmic side of the detector. The 127 hexagons represent individual detector elements.

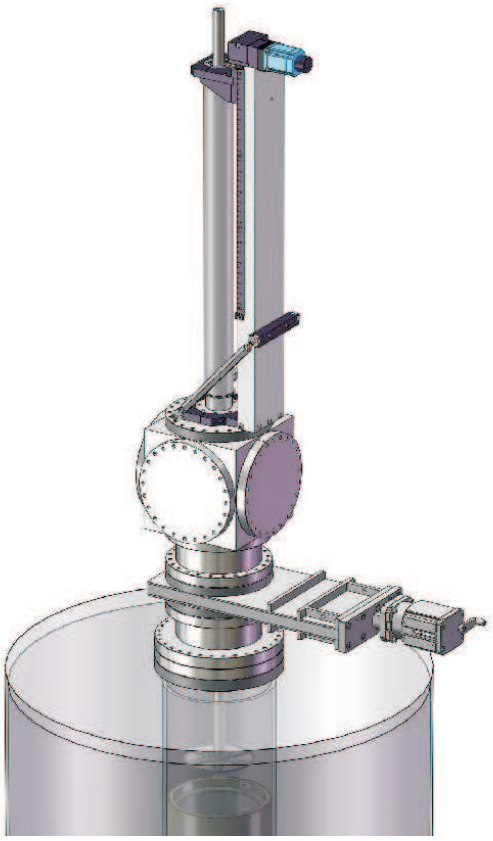

Figure 13: Right: design of the detector housing, which allows the detector to be retracted for servicing without the need to break the vacuum, nor to warm up the magnet.

The hexagonal detector elements in the preliminary design have sides of length $s_d = 5.2\,\text{mm}$ and area of $A_d = 0.70\,\text{cm}^2$. There are several reasons for this choice. First, the electron-proton separation of the initial impact position on the detector can never be more than 4 mm (or 5.2 mm for the measurement of b, where we are also interested in downward-going protons). Our choice of $s_d = 5.2\,\text{mm}$ guarantees that the electron is never more than one detector element away from the proton. This means that only 14 detector elements (including conjugate elements on the opposing detector) need to be considered in constructing a coincidence event. Similarly, only 14 elements need be considered in searching for an event where an electron reflects from a detector and then stops, either in the same detector or the opposing detector. Second, the noise gain of the preamplifier increases with detector capacitance, while the speed decreases. With our choice of $A_d = 0.7\,\text{cm}^2$, the parallel plate capacitance of one element is approximately 6 pF. Inter-pixel capacitance and contributions from the electrical interconnects will bring the total capacitance to approximately 10 pF, which is acceptably small. Finally, the number of detector elements, 127 per detector, does not require an unacceptably large number of electronic channels.

It is important to note that, though the detector is segmented, there are no dead spaces between the detector elements. Even though there is a gap of 100 μm between the metal pads for adjacent elements, *all* charge deposited in the active volume of the detector is collected,

though it may be shared among adjacent elements. This property guarantees that if a proton hits within the interior hexagons in Fig. 12, the corresponding electron must hit within the active area (interior plus perimeter hexagons) of the same (or opposing) detector.

Micron Semiconductor has constructed prototype detectors that fulfill all of the design criteria. The detector will be mounted on a ceramic support, suitable for cooling to cryogenic temperatures. Behind the ceramic support will be a circuit board with individual FETs, as well as feedback resistors and capacitors for each detector channel.

Prototype detectors are available in different thicknesses. We obtained a prototype with the full thickness of 2 mm only recently, and did all tests to date with thinner detectors and α sources. We plan to verify their sensitivity for protons at 30 keV at the proton accelerator at the Space Science/ISR department at LANL within the first two months of 2010.

In principle, the small thickess of the dead layer of 100 nm of silicon should allow for fully efficient proton detection. Equally, the thickness of the detector (in the range from 300 μm to 2 mm) should only matter insofar as it changes the electrical capacitance, rendering proton detection easiest with the thickest detector. Therefore, it is sufficient to prove proton detection with the thin test detectors (which are ready to be used).

Further detector testing is planned at LANL and at the University of Manitoba in later stages of the project for optimization, and to establish the insensitivity of the proton efficiency on the impact parameters (energy, angle, position) of the proton.

As the magnet bore will be at low temperature, a load-lock mechanism is necessary at each end of the magnet to remove the detectors for servicing. Fig. 13 shows a preliminary design for such a mechanism. HV insulation is not shown. The detector package, including front end electronics and cabling, is mounted to the end of a shaft driven by a linear positioner. In the extended position, the detector is correctly located within the magnet bore at its operating position. For servicing, the linear position is retracted placing the detector within a service chamber. A gate valve is closed to isolate the magnet vacuum and the detector can then be accessed or removed through a flange on the service chamber. The linear positioner ensures reproducible positioning of the detector. All components of the load-lock are non-magnetic.

4. The data acquisition system

We are planning to use a DAQ system based on the digital processing of the detector signals (DSP), described in more detail below. In particular, the proposed experiment requires a DAQ system which does not introduce any systematical bias in the data, and offers a low electronic threshold as well as good timing resolution for the 256 synchronized channels. Among other options, practical DSP expertise has been acquired at the ORNL Physics Division by the Decay Spectroscopy Group, running a 20-board (80-channels) set of Digital Gamma Finder modules [39]. These universal boards produced by the X-ray Instrumentation Associates (XIA) have been routinely used in charged particle and gamma spectroscopy [40] at ORNL and at other laboratories. The proposed board, PIXIE-16, has the following characteristics:

- 100 MHz, 12 bit digitizing ADC for each channel,
- 16 channels on one board, using 1 FPGA chip for every four channels,

- fixed, low-noise analog conditioning (selectable amplification and offset adjustment for each channel),
- FIFO memory to store pulse shapes, up to 80 μs long,
- multichannel trigger bus line, and
- based on PCI architecture which allows very high data transfer at 100 MBytes/s

Each channel features real-time processing algorithms to determine amplitude and arrival time. This analysis is using fixed width trapezoidal filters (moving average filter) with continuous baseline monitoring and correction for exponential pulse decay. On-board storage capacity will allow us to record up to 80 μs long pulses for pile-up correction and precise timing/pulse shape analysis. Sixteen boards of 16-channel PIXIE-16 are needed to instrument 256 channels of the pixelated silicon detector. With a predicted rate of about 2500 Hz of detected neutron decays, the amount of transferred data will be moderate, however a large amount of storage will be required.

The readout and data storage will be managed by a host computer installed on the PCI chassis. The role of this central CPU will be to organize data buffers from individual cards, and to send the data to the storage. Additional CPUs will analyze a fraction of the data online. The data stream consists of time-stamped energies and traces containing a section of the pulse around its rising edge. The energies will be computed with real time processing algorithms on the PIXIE-16, using a trapezoidal filter. A block diagram of the complete proposed DAQ system is shown in Fig. 14.

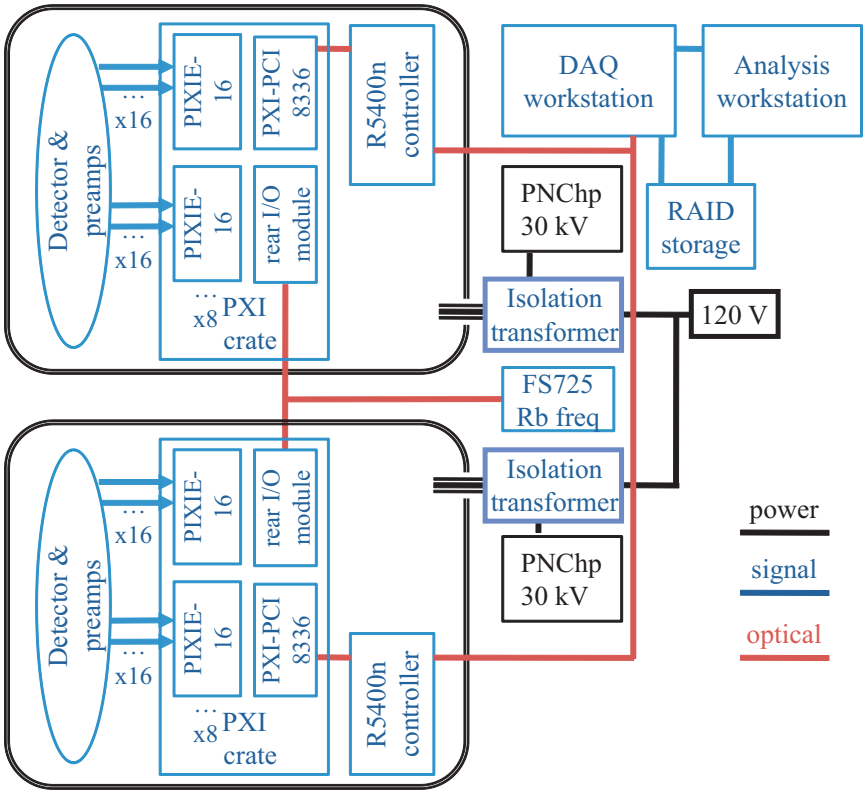

Figure 14: Block diagram of the DAQ system, described in the text.

5. Dominant uncertainties in the determination of *"a"*

The neutrino–electron correlation coefficient a is determined in a χ^2-fit to the two dimensional function P_t, introduced in Eq. (11), which depends on t_p, proton TOF, and on E_e, electron energy. The fitting parameters are: a, N, the number of decays, b, the Fierz interference term, and eventually additional parameters which characterize spectrometer properties.

Our plan is to analyze our data first, and to the best extent possible, with method B, introduced in Sec. 2 and in the original Nab proposal [33]. In this method, our knowledge of the spectrometer properties, as determined from auxiliary measurements, is converted into a prediction of the shape of $\Phi(1/t_\mathrm{p}^2, p_\mathrm{p}^2)$. We perform the fit twice: First, we use the full data set and two additional fit parameters, the average value of the detection function (parametrized as length of flight path L), and an electron energy calibration factor (E_cal). In a second step, we fix the additional parameters, and reduce our data set by taking only the inner 70% of the data in the $P_t(1/t_\mathrm{p}^2)$ distribution for each given electron energy E_e. This procedure makes use of the fact that the edges of $P_t(1/t_\mathrm{p}^2)$ distribution are mainly sensitive to the shape of the detection function $\Phi(1/t_\mathrm{p}^2, p_\mathrm{p}^2)$, and the inner part is mainly sensitive to the neutrino electron correlation coefficient a. The decision to use only the inner 70% of the data sample in the second fit reduces the statistical sensitivity by 65%, which is offset by considerably relaxed tolerances for a number of false effects (sources of systematic uncertainty).

The statistical uncertainty is shown in Table 1 for several possible threshold values for the electron energy ($E_\mathrm{e,min}$), and $t_\mathrm{p,max}$, a high proton TOF cutoff due to accidental coincidences. N is the number of decays in which the proton goes into the upper detector, irrespective of further cuts.

Table 1: Statistical uncertainty in the determination of a in Method B, and the influence of different cuts.

lower E_e cutoff:	none	100 keV	100 keV	300 keV
upper t_p cutoff:	none	none	100 μs	40 μs
σ_a	$2.4/\sqrt{N}$	$2.5/\sqrt{N}$	$2.5/\sqrt{N}$	$2.5/\sqrt{N}$
σ_a (E_cal, l variable)	$2.5/\sqrt{N}$	$2.6/\sqrt{N}$	$2.6/\sqrt{N}$	$2.7/\sqrt{N}$
σ_a (inner 70% of data)	$4.1/\sqrt{N}$	$4.1/\sqrt{N}$	$4.1/\sqrt{N}$	$4.1/\sqrt{N}$

Omission of b, i.e., setting $b \equiv 0$ for a fit within the standard model, would not improve the uncertainty in a. A total of 1.6×10^9 events are required to determine a with a relative statistical uncertainty of 10^{-3}. About 8 weeks of live data taking are needed for a single run, without extra measurements devoted to systematic checks.

We now turn to the most important associated systematic uncertainties:

(a) **Magnetic field: field shape in the filter region**

The main contribution to the width of the detection function comes from the curvature of the magnetic field in the filter region. The measurement of the curvature is done by

field mapping, which is simplified by the fact that this measurement is both relative in the measured magnetic field values and in the position. The main cause of uncertainty will be that the field curvature changes by 8% as a function of the radial coordinate of the magnetic field line. However, a direct measurement of the position of the projection of the center of the filter region onto the detector will be used to determine the field curvature to 1%, which translates into a relative uncertainty in a of 5×10^{-4}.

(b) **Magnetic field: magnetic field ratio between TOF region and the filter region (r_{B})**

The calibration of the Hall probe(s) will be determined to better than 10^{-3}. The limiting factor in the determination is the variation of the magnetic field with the radius in the filter region. The magnetic field at the center of the filter region (the pinch) is about 6% lower than the magnetic field maximum for the magnetic field line with the highest radius which still intersects the detector face. We assume a measurement uncertainty in r_{B} of 1%, and then we obtain a relative uncertainty in a of 2.5×10^{-4}.

(c) **Magnetic field: magnetic field ratio between decay volume and the filter region ($r_{\mathrm{B,DV}}$)**

The magnetic field ratio between the decay volume and the filter region, $r_{\mathrm{B,DV}}$, can be determined very precisely with the second method shown in Appendix D (see Eq. (41)). The biggest uncertainty will be the position dependence of the magnetic field at the filter. This dependence is recorded in the data thanks to the position dependence of the detector. We expect that this reduces the uncertainty to 10% (of the variation of 6%), and obtain a relative uncertainty in a of 3×10^{-4}.

We note that this procedure allows us to determine the projection of the field pinch along the central field line onto the detector *in situ*, and can thus be used to analyze the sources of systematic uncertainty discussed above.

(d) **Length of the TOF region**

The upper end of the TOF region marks the onset of the strong electrostatic acceleration just below the detector. The length of the TOF region will be determined in a fit to the edges of the $P_t(1/t_{\mathrm{p}}^2)$ distribution. Therefore, it contributes (weakly) to the statistical, but not to the systematic uncertainty.

(e) **Homogeneity of the electric potential in the decay and filter regions**

The electric field profile in a volume surrounded by conductors is calculated with computer codes, which are able to model the geometry. If the required accuracy in the homogeneity of the electric potential is less than a few volts, surface effects have to be included. The work function of metals is typically $W \sim 4 - 5\,\mathrm{eV}$ [42]. For a given metal, it depends on the crystalline orientation at a level of about 0.3 eV. This becomes a problem if different surface materials, orientations, or just "dirty" surfaces are present. Possible inhomogeneities of the work function at the electrode surface or surface charges influence the electric field distribution. Surface charges can remain

on metallic surfaces if there is a non-conductive oxide or dirt layer on them. We are using the term "surface voltage" for the combined effect of work function and surface charges.

Surface voltage variations of order of 100 mV have been found in the *a*SPECT experiment [43]. The length scale of this variation is about 5 cm, so only limited averaging can be expected for the potential of the inner side of a cylindrical electrode. Ref. [44] discusses observed surface charging on metallic conductors due to radiation, an additional effect that has to be considered. At radiation levels which are many orders of magnitude higher than in Nab, the effect can be as big as several volts.

Implementing an optimized surface coating can yield an inhomogeneity of better than 10 mV [45], which can be verified with a Kelvin probe. An electrostatic potential inhomogeneity of 10 mV between the decay and filter regions would cause a relative shift in a of 5×10^{-4}.

(f) **Homogeneity of electric potential in the TOF region**

Since proton and electron momenta in the TOF region are well longitudinalized (oriented along the magnetic field), the sensitivity to electric potential homogeneities is much lower here. An inhomogeneity of 10 mV would cause a relative shift in a of 1×10^{-4}.

(g) **Neutron beam: center of the decay volume**

The vertical position of the neutron beam in the spectrometer coordinate frame can be determined with a position sensitive detector with an accuracy of 2 mm or better. A height shift of the neutron beam by 2 mm would cause a relative shift in a of 4×10^{-4}. The position of the detected neutron decays in the horizontal plane causes no additional uncertainty, as it is mapped onto the main detector, which is position sensitive.

(h) **Neutron beam: profile**

The vertical extent of the neutron beam profile can be determined with a position sensitive detector with an accuracy of 1 mm or better. This translates into a relative uncertainty in a of 2.5×10^{-4}.

In the plane perpendicular to the neutron beam direction, the neutron beam profile changes considerably over the decay volume. This is also mapped onto the main detector. The beam profile is a concern due to the edge effect: because of the gyration of protons and electrons around the magnetic field lines, the decay volume (the volume in which neutron decays are detected by the main detectors) is not sharply bound. Consequently, the detection efficiency for neutron decays at the boundaries is a function of position and gyration radius. The gyration radius is a function of proton momentum p_{p} and $\cos\theta_0$. An exact calculation requires the specification of a complete neutron beam design, which is not yet completed. Even so, the work in Refs. [41, 43, 46] shows that the edge effect is important, but can be made small.

(i) **Neutron beam: Doppler effect**
Our initial estimates indicate that the Doppler effect is most likely negligible since the neutron beam is transverse to the spectrometer axis. Hence, it should be possible to take it into account with sufficient precision. The Doppler effect is on the simulation agenda, and will be analyzed in due course.

(j) **Adiabaticity of proton motion**

It is not necessary that the electron and proton orbits in our spectrometer are calculable in the adiabatic approximation, but it simplifies the construction of an effective spectrometer model. The condition of the adiabatic approximation can be formulated as the requirement that ϵ, a quantity, defined in [47] as:

$$\epsilon = \frac{p\frac{\partial B}{\partial z}}{eB^2} \tag{16}$$

be small. In appendix C we show that the effect of the non-adiabaticity of the proton motion on the proton TOF causes an uncertainty in a. However, we consider this effect to be calculable to at least 20% accuracy, so that we assign a relative uncertainty in a of 1×10^{-4}. We can test the calculation straightforwardly by running the spectrometer at a different magnetic field.

(k) **Main detector: electron energy calibration**

The electron energy calibration of the main detector will be performed with several monoenergetic conversion electron sources. The electron energy calibration can be inferred from the position of the edges of the $P_t(1/t_{\mathrm{p}}^2)$ distribution. We will treat the conversion factor between the electron energy and pulse height as a fit parameter. However, we plan to prove with calibration sources, and with the analysis of the position of the distribution edges, that non-linearities are absent or understood at a level of well below a keV.

(l) **Main detector: trigger efficiency**

We will be working with ion-implanted Si detectors with a 100 nm thick dead layer. The proton impact energy is given by the proton acceleration voltage (planned to be 30 kV) plus the initial kinetic energy. In this case, the trigger efficiency for protons in the Si detector is expected to be about 98%. The missing 2% are due to backscattering, and depend on the size and the material of the dead layer. The imperfect trigger efficiency is a problem, as it depends slightly on the proton impact energy, which causes a distortion of the $P_t(1/t_{\mathrm{p}}^2)$ distribution. GEANT simulations have demonstrated that the average energy loss in the dead layer is about 11 keV. We assume that the detector noise level allows us to set a threshold at a pulse height of half of the average proton pulse amplitude. In that case the energy dependence of the proton trigger efficiency becomes 130 ppm/keV. Assuming, that we can verify this to only 50% accuracy in a dedicated test at the proton source in Manitoba, we would have a relative uncertainty in a of 2.5×10^{-4}.

The trigger efficiency for electrons is essentially 100% above a cutoff energy given by the electromagnetic field design, as backscattered electrons are guided by the magnetic

field. They are either directed to the opposite detector, or reflected only to arrive back at the same detector.

(m) **Residual gas**

Electrons are less affected by the residual gas than protons. The proton TOF is altered after residual gas ionization or scattering. Furthermore, these processes, or charge exchange, might remove the proton altogether. Residual gas composition and density are the relevant parameters. GEANT simulations demonstrate that associated changes in the extracted value of a are tolerable if the residual gas pressure can be reduced to 10^{-8} torr independent of the type of gas, and negligible if we can reduce the residual gas pressure to 10^{-9}. Most of the vacuum system consists of the inner bore of a superconducting magnet, which would be destroyed by baking. However, outgassing is strongly reduced by keeping the inner bore at about 70 K. It would be meaningless at the present stage to assign an uncertainty in a caused by the effect of the residual gas. The vacuum system and the planned pumping scheme are somewhat similar to the aSPECT experiment, in which a vacuum level of 7×10^{-9} torr was reached [48].

We plan to verify the GEANT calculations by introducing small known amounts of gas into the vacuum vessel.

(n) **Background**

Environmental background (every background caused by a process which is not neutron beam related) is expected to be small. In the asymmetric design, we have no deep Penning trap. We expect the main cause of environmental background to be electronic noise on the detector. The amount of electronic noise is a strong function of the threshold setting. The amount of singlex background sets a limit on the time we can wait for the proton to appear in either detector after we have detected the electron from the same decay. We estimate that a waiting time of 40 μs is possible without a significant amount of accidental coincidences.

Neutron beam related background rates are difficult to estimate because they depend sensitively on the design of the experiment, in particular the collimation system, shielding, and beam stop. These aspects of the experiment will have to be carefully optimized. Having said this, we are still trying to estimate the amount of beam related background in the following way. About 3×10^{-8} of the neutrons that come out of the beam guide decay in our decay volume. The other neutrons are absorbed in the collimation system or in the beam stop by diaphragms made of ^{6}LiF. In this process, neutron and γ background is produced at the 10^{-4} level [49]. The background is further reduced by shielding ($< 1\%$), the solid angle ($\sim 10^{-4}$), and the efficiency ($< 5\%$) of our detectors, so that we expect the background rate to be smaller than the signal rate.

An important feature of the Nab experiment is the detection of both proton and electron from the neutron decay in coincidence. We conducted a demonstration of this technique by observing electron-proton coincidences from neutron decay using a silicon surface-barrier detector coupled to the NIST lifetime apparatus [50]. A 30 keV potential was used to accelerate protons. The detector area was approximately the size

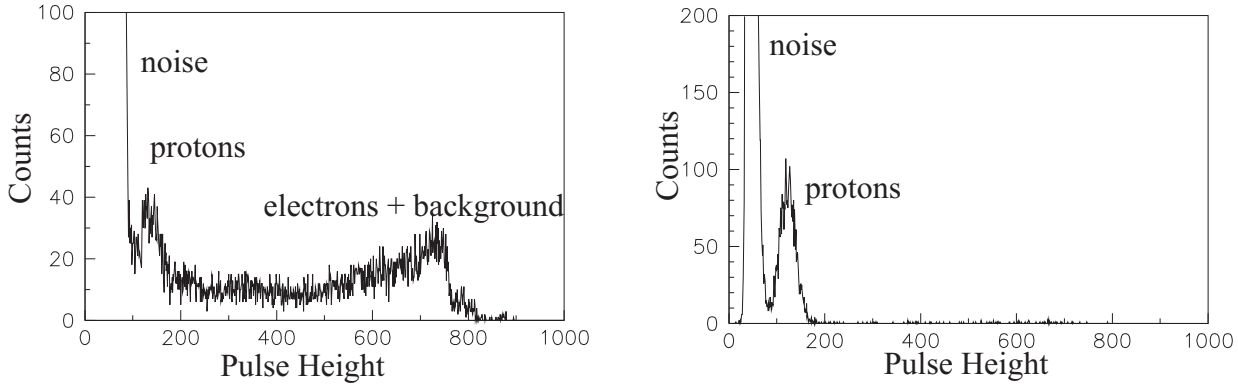

Figure 15: Plots of protons from neutron decay in singles (left) and coincidence from a test measurement at NIST. See the text for details.

of one pixel of the Nab detector. The geometry was farther from optimal than the Nab configuration, as the detector was placed much closer to the neutron beam and the final collimator ($\sim 10\,\mathrm{cm}$). Since the NIST lifetime experiment was designed to count decay protons after the neutron beam is shut off, this was not a limitation for their experiment. Figure 15 illustrates the effect of the coincidence requirement on suppressing backgrounds. The left-hand plot shows the observed singles spectrum. The 30 keV proton peak can be clearly seen, as well as electronic noise, the (distorted) electron spectrum, and background events. The electron spectrum is distorted because the detector was only $300\,\mu\mathrm{m}$ thick, far too thin to stop all of the electrons. The right-hand plot shows a spectrum of proton energy in coincidence with decay electrons, greatly suppressing backgrounds. The rates of false coincidences due to these backgrounds are discussed above.

We are aware that a neutron beam is typically surrounded by a halo. The halo neutrons can hit surfaces in the spectrometer that are not covered with ^{6}LiF, and thus produce a background whose intensity can exceed that of the direct background if the latter is shielded well. The likely origin of the halo is scattering on the edges of the diaphragms or on impurities in them. Our strategy is to cover most surfaces seen by the neutron beam with neutron absorbing material. We can do this where it matters most, i.e., in the collimation system and before the beam stop. However, we cannot cover the electrode system. If the halo causes too much secondary background, we can always collimate the neutron beam earlier and harder.

Some of the sources of uncertainties, if underestimated, would show up as a deviation of the expected $P_t(1/t_\mathrm{p}^2)$ distribution. Specifically, the effects of possible electric field inhomogeneities in the decay, filter and TOF regions, and the effect of the residual gas, are strongly enhanced at very low values of $1/t_\mathrm{p}^2$. The measurement of the known spectral shape of the $P_t(1/t_\mathrm{p}^2)$ distribution (which is linear in the central region) provides additional control over the systematic effects.

Table 2 summarizes the main uncertainties in the determination of a. Some sources of uncertainty are marked with an asterisk. These parameters can be determined from the edges of the $P_t(1/t_\mathrm{p}^2)$ distribution in the primary data, so a separate dedicated measurement

is not necessary.

Table 2: Systematic uncertainties in the determination of a due to imperfect knowledge of spectrometer properties in Method B. Parameters marked with asterisks can be determined from the edges of the $P_t(1/t_\mathrm{p}^2)$-distribution in the primary data, so a separate dedicated measurement is not necessary. The uncertainties are added in quadrature to obtain the total.

Experimental parameter	Systematic uncertainty $\Delta a/a$
Magnetic field	
... curvature at pinch	5×10^{-4}
... ratio $r_\mathrm{B} = B_\mathrm{TOF}/B_0$	2.5×10^{-4}
... ratio $r_\mathrm{B,DV} = B_\mathrm{DV}/B_0$	3×10^{-4}
Length of the TOF region	(*)
Electrical potential inhomogeneity:	
... in decay volume / filter region	5×10^{-4}
... in TOF region	1×10^{-4}
Neutron Beam:	
... position	4×10^{-4}
... width	2.5×10^{-4}
... Doppler effect	small
Adiabaticity of proton motion	1×10^{-4}
Detector effects:	
... Electron energy calibration	(*)
... Trigger efficiency	2.5×10^{-4}
Residual gas	small
Background	small
Sum	1×10^{-3}

Analysis Method A will go beyond what can be achieved with Method B: We will reconstruct the detection function in much more detail from the shape of the measured $P_t(1/t_\mathrm{p}^2)$ distribution. This approach introduces more free parameters; we rely on Method B to get good starting values for them, otherwise the fitting procedure which determines the optimum value for the free parameters may not be numerically stable. The choice of the parameters and their functional relationship to the detector response function are discussed in App. A. Here we discuss the philosophy behind Method A.

For a spectrometer with a point-like source, and without an electric field to accelerate and detect the protons, the relationship between t_p, the proton time of flight, and p_p, the momentum, is a simple one:

$$p_\mathrm{p} = \frac{m_\mathrm{p} L}{t_\mathrm{p}} f(\cos\theta_0)\,, \tag{17}$$

where m_p is the proton mass and L the length of the flight path, and $f(\cos\theta_0)$ is given in Eq. (15). If we independently calculate $m_\mathrm{p}L/t_\mathrm{p}$, the unobserved quantity $\cos\theta_0$ creates an

uncertainty in $p_{\rm p}$. The above simple relations are subject to these further restrictions:

(i) the product of $p_{\rm p}$ and $t_{\rm p}$ is constant if these variables are taken from the edges of the time distribution measured for fixed a electron energy, $E_{\rm e}$, and

(ii) a universal resolution function describes all edges.

In App. A we show that the effects of an electric field can be brought into the same form as above. Method A follows these steps:

(a) We construct a function of the time of flight, $p_{\rm p}(t_{\rm p})$, that gives the proton momentum. The five parameters needed to specify the function can be determined from the location of the edges in the proton energy spectra for fixed electron energy or from measured spectrometer properties, distances, field strengths, etc.

(b) If the proton momentum is calculated from $p_{\rm p}(t_{\rm p})$, the shape of the proton edges is given by a universal resolution function. The same parameters, η, ρ, and H are needed to describe the distribution of $p_{\rm p}$ both with and without the electric field.

(c) If the spectrometer parameters are determined from external measurements, systematic uncertainties are introduced by the uncertainties in the measurements. Determining the parameters from fits to the same data set that determines a, has the consequence of increasing the statistical uncertainty in a. If the resolution function is narrow, both kinds of uncertainties are small. We estimate that if the spectrometer energy resolution is 3%, the increase in the statistical uncertainty in a is 10%. The analytical framework presented in App. A shows how to analyze the issues of describing the spectrometer response function in order to quantify systematic uncertainties and develop an optimal strategy of measurement and *in situ* fitting of spectrometer properties.

A successful application of Method A would substantially reduce the systematic uncertainties given in Table 2.

6. Dominant uncertainties in the determination of *"b"*

Careful attention to understanding details of the spectrometer response to both protons and electrons discussed above also helps to reduce the systematic uncertainties in the measurement of b. Measuring b amounts to a precise determination of the shape of the electron spectrum and its deviation from the $b = 0$ shape predicted by the standard model. Any such deviation will be far more pronounced at low electron momenta than for high momenta. Therefore the accurate understanding of background rates, which increase with decreasing pulse size, is crucial. The coincidence method will help us to reduce the background rates. Momentum dependence of electron detection efficiency, especially near threshold, and electron spectrum distortions due to reflections at the detector surface and elsewhere in the spectrometer, must be controlled. The calibration methods outlined above generally bring us to the desired level. We have initiated work on a realistic Monte Carlo simulation of the background. Such simulations can only be taken as a guideline; eventually the backgrounds will have to be measured and dealt with *in situ* because of the complexity of the apparatus.

Table 3: Statistical uncertainty in the determination of the Fierz Interference term b, and the influence of an electron energy cut.

lower E_e cutoff:	none	100 keV	200 keV	300 keV
σ_b	$7.5/\sqrt{N}$	$10.1/\sqrt{N}$	$15.6/\sqrt{N}$	$26.4/\sqrt{N}$
σ_b ($E_{\rm cal}$ variable)	$7.7/\sqrt{N}$	$10.3/\sqrt{N}$	$16.3/\sqrt{N}$	$27.7/\sqrt{N}$

The statistical uncertainty in b is given in Table 3, which is in agreement with the calculations of Ref. [20]. Here, again, N is the number of neutron decays. N is not restricted to the subset where electron and proton pass the respective cutoff conditions. The statistical uncertainty of b increases quickly if a high electron energy cutoff is chosen. The reason is that at higher electron energies a non-zero value of b looks similar to a change of the normalization N. Therefore, the fitting parameters N and b are strongly correlated.

The second line of Table 3 lists the statistical uncertainty in b if the energy calibration is determined from a fit to the beta spectrum. The statistical uncertainty is not significantly worse than that obtained with a fixed energy calibration.

For an overall sample of 5×10^9 decays, the statistical uncertainties σ_b calculated on the basis of the above table are in the range of $\sigma_b \sim 10^{-4}$, far better than our goal of overall uncertainty of $\sim 10^{-3}$. It is clear that the main challenge in the measurement of b will be in the systematics. While we have indicated strategies for controlling the systematics, a major contribution will be the electron background, which will ultimately have to be evaluated and dealt with *in situ*.

7. Nab spectrometer and experiments with polarized neutrons

The asymmetric Nab spectrometer can be used for subsequent polarized neutron decay experiments, abBA and PANDA. The basic setup is shown in Fig. 16. Here we discuss only the differences between the asymmetric configuration and the originally proposed symmetric one. Knowledge of the degree of polarization of the neutron beam is an important systematic uncertainty for both proton and electron asymmetry, independent of the spectrometer design.

For the discussion of the statistical sensitivity, we need to consider the "visible" decay rate (see section 2), but also the enhanced sensitivity of an asymmetry of the type

$$\text{differential decay rate} \propto (1 + \alpha \cos\theta_0) \tag{18}$$

to the choice of the accepted solid angle. In Eq. (18), θ_0 is the angle of electron (or proton) emission relative to the neutron beam polarization (i.e., the magnetic field) at the moment of the neutron decay, while α designates the size of the asymmetry, as follows. For the electron count rate asymmetry, we express the differential decay rate as a function of the electron energy and set $\alpha = A \cdot v/c$. For the proton asymmetry, we will integrate the differential decay rate over proton and electron energies, and set $\alpha = C$. We further note that it is possible to measure the proton count rate asymmetry as a function of the electron energy. In this case α becomes a function of A, B and the electron energy, as given in Ref. [51],

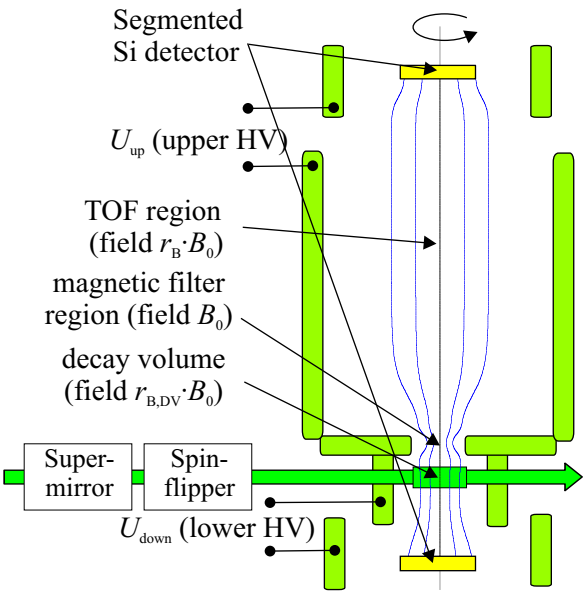

Figure 16: Sketch of the asymmetric spectrometer, configured for measurements with a polarized neutron beam; not to scale.

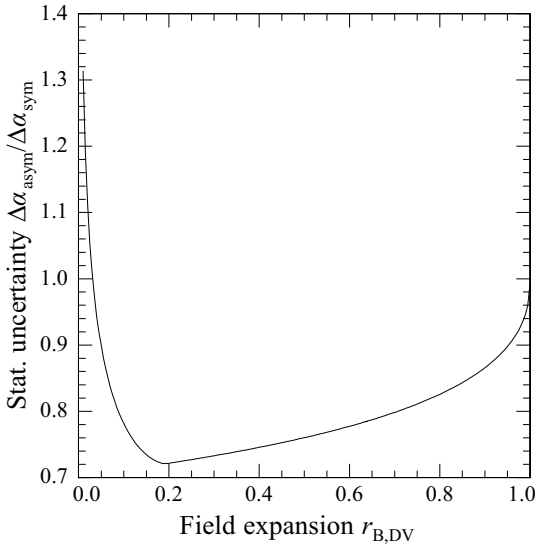

Figure 17: Statistical sensitivity: statistical uncertainty in a polarized experiment will be somewhat reduced in the asymmetric design.

and can be used to make a precise determination of B. The enhancement of the statistical sensitivity due to a restriction of the accepted solid angle is discussed at length in Ref. [41]. The enhancement of the statistical uncertainty for our asymmetric spectrometer is depicted in Fig. 17. The figure assumes a decay volume of 60 cm^3 for the symmetric configuration [52], the decay volume of the asymmetric configuration as shown in Fig. 9, and it assumes that $\alpha < 1$, which is a good approximation for the beta asymmetry and a reasonable one for the proton asymmetry.

PERKEO II [15], the most recent experiment which measured A, the beta asymmetry, could have been carried out using just one electron detector if it were not for the events in which the electron back-scatters from the detector. The second detector is necessary to detect the electron energy missing in the first detector, and thus to ensure the correct measurement of the full electron energy for such events. Naturally, the two detectors detected more events than one alone would have; however, this effect of the increased number of counts is already accounted for in Fig. 17. The individual results of the two detectors in PERKEO II in principle differed slightly due to neutron beam fluctuations, and because of the magnetic mirror effect. The potential discrepancy due to neutron beam fluctuations can be removed by means of a continuous beam monitor. In the asymmetric configuration there is no equivalent to the magnetic mirror effect: the reflection of particles from the magnetic field pinch (the filter) is there by design and not unwanted. Therefore we do not anticipate that the asymmetric design will produce an unexpected problem of a similar nature in the determination of the asymmetries.

The measured asymmetry for a decay rate as in Eq. (18) is

$$\alpha_{\rm exp} = \frac{N^{\uparrow} - N^{\downarrow}}{N^{\uparrow} + N^{\downarrow}} = \alpha \, \overline{\cos\theta_0} \, . \tag{19}$$

We label the count rates in the upper detector $N^{\uparrow}$ and $N^{\downarrow}$ for the different neutron spin states. In the adiabatic approximation, decay particles are detected in the upper detector if their emission angle fulfills the condition $\cos\theta_0 > \cos\theta_{\min}$ (see Eq. (14) and the discussion in App. C). Given that $\cos\theta_0$ is uniformly distributed, the average electron emission angle is:

$$\overline{\cos\theta_0} = \frac{1}{2}\left(1 + \sqrt{1 - r_{\mathrm{B,DV}}}\right) . \tag{20}$$

For $r_{\mathrm{B,DV}} \approx 0.5$, a relative error in the magnetic field ratio of $\Delta r_{\mathrm{B,DV}}/r_{\mathrm{B,DV}} \approx 0.5\%$ translates into a relative error in α of $\Delta\alpha/\alpha = 10^{-3}$. We do not have to rely on field maps to measure magnetic field ratio $r_{\mathrm{B,DV}}$; instead, we can use the measured decay rates to find it experimentally. We add the subscripts "U" and "D" for upper and lower detector, and make use of the fact that the two detectors see opposite solid angles; we obtain

$$\overline{\cos\theta_{0,\mathrm{U}}} = \overline{\cos\theta_{0,\mathrm{D}}} + 1 . \tag{21}$$

We can replace the determination of α through use of Eq. (19) by

$$\alpha_{\mathrm{exp,U}} - \alpha_{\mathrm{exp,D}} = \frac{N_{\mathrm{U}}^{\uparrow} - N_{\mathrm{U}}^{\downarrow}}{N_{\mathrm{U}}^{\uparrow} + N_{\mathrm{U}}^{\downarrow}} - \frac{N_{\mathrm{D}}^{\uparrow} - N_{\mathrm{D}}^{\downarrow}}{N_{\mathrm{D}}^{\uparrow} + N_{\mathrm{D}}^{\downarrow}} \equiv \alpha . \tag{22}$$

The sensitivity of this expression to α is about the same as Eq. (19). Equations (21) and (22) are strictly valid only if the magnetic field ratio $r_{\mathrm{B,DV}}$ does not depend on the position. However, $r_{\mathrm{B,DV}}$ will decrease with the distance of the decay point from the symmetry axis, and will depend, to a lesser extent, on the z coordinate of the decay point. We show in App. D that the error we make by using Eqs. (21) and (22) for inhomogeneous fields is small.

Furthermore, we can determine the average emission angle with

$$\overline{\cos\theta_{0,\mathrm{U}}} = \left(1 - \frac{A_{\mathrm{exp,D}}}{A_{\mathrm{exp,U}}}\right)^{-1} . \tag{23}$$

We have to do this with electrons, as only one detector would be sensitive to protons.

In the measurement of the beta asymmetry, we choose to detect all protons in order to suppress the background. We plan to use the same electrostatic configuration as for the measurement of the Fierz parameter b: lower detector at $-30\,\mathrm{kV}$, and the remainder of the spectrometer at ground potential, plus a mirror voltage of $+1\,\mathrm{kV}$ in the filter region or at the other detector (see Fig. 7).

In the measurement of the proton asymmetry, we plan to detect protons only in the upper detector. The upper detector would be at $-30\,\mathrm{kV}$, and the remainder of the spectrometer at ground potential. We would have to use Eq. (23) to determine $\overline{\cos\theta_{0,\mathrm{U}}}$, and then use Eq. (19) to get the proton asymmetry C. The proton asymmetry is sensitive to electric potential inhomogeneities. In the symmetric configuration, having the decay volume in an (unwanted) electrostatic potential trap only 1 mV deep, increases the measured proton asymmetry by 0.17% (the error increases with the square root of the trap depth). An unwanted potential gradient is equally bad, but the effect cancels here to the first order

if the average of the measured asymmetry between upper and lower detector is evaluated. It is possible to reduce the sensitivity to an electrostatic potential trap if the analysis is restricted to certain proton or electron energies in order to avoid the low-energy protons. For the asymmetric configuration, the sensitivity to electric potential traps is practically absent: An (unwanted) electric potential of 500 mV of the filter plane relative to the decay volume changes the proton asymmetry by less than 0.04% (for $r_{\mathrm{B,DV}} = 0.5$).

8. Organization and schedule

The funding application is separated into several parts. The first part consists of the equipment needed specifically for the Nab experiment. The necessary modifications of the FNPB beamline to accommodate the beta decay experiments are given as work package B1. The last part comprises the spectrometer magnet, which is needed for Nab, but also for any follow-up experiments with polarized neutrons (abBA and/or PANDA). We have listed below the tentative division of the main institutional responsibilities, including assignments to subproject participants.

The Nab collaboration effort is led by the two Spokespersons, an Experiment Manager, an On-site Manager, and the Executive Committee. Memoranda of understanding between the participating institutions are in preparation. The work package breakdown structure of the request for the Nab experiment is shown in Table 4.

Table 4: Top-level subproject structure, responsible institutions, and responsible persons of the Nab project request.

	Subproject	Resp. institution(s)	Resp. person(s)
1	Beamline	UT	G.L. Greene
2	Shielding and utilities	ORNL	S.I. Penttilä
3	Detectors	LANL	W.S. Wilburn
		UVa	D. Počanić
		U Manitoba	M.T. Gericke
		U Winnipeg	J. Martin
4	DAQ	UKy	C. Crawford
5	Electrode System	ORNL	J.D. Bowman
6	Vacuum system	UVa	S. Baeßler
7	Magnetic field measurement	UVa	D. Počanić
8	Project management for Nab	ORNL	S.I. Penttilä
B	Beamline modification	ORNL	S.I. Penttilä

The work package breakdown structure of the request for a superconducting magnet is shown in Table 5.

An integral part of this proposal is a separate work breakdown structure (WBS) dictionary showing in detail how the Nab experiment costs were estimated for this update.

Table 5: Top-level subproject structure, responsible institutions, and responsible persons of the spectrometer magnet request. The spectrometer magnet work package will be lead by the institution placing the order.

	Subproject	Resp. institution(s)	Resp. person(s)
M1	Spectrometer magnet	UVa	S. Baeßler, D. Počanić
		ORNL	S.I. Penttilä
M2	Passive anti-magnetic screen	ASU	R. Alarcon
M3	Project management	ORNL	S.I. Penttilä

Table 6: Project milestones of the Magnet Project. The principal milestones that lie on the critical path are shown in boldface.

	Milestone	Completion
0.a	Start of project	Jul 2010
0.	**Magnet design ready for bidding**	**Jul. 2010**
1.a	Order for magnet placed (design & option to build)	Nov. 2010
1.b	Acceptance of engineering drawings	Sep. 2011
1.c	Delivery of magnet	Dec. 2012
1.	**Spectrometer magnet accepted**	**March 2013**
2.a	Passive Anti-Magnetic screen: Magnetic design finished	Dec. 2011
2.	**Passive Anti-Magnetic screen built**	**Dec. 2012**

ASU and UVa are planning to seek spectrometer magnet funding in an NSF-MRI; however there is no *a priori* assurance for NSF MRI's.

Table 7: Nab project milestones. The principal milestones that lie on the critical path are shown in boldface.

	Milestone	Completion
0.a	Detector prototype detects protons	April 2010
0.	**Start of project:**	**Sep. 2010**
1.a	Magnetometer calibrated	Sep. 2011
1.b	Magnetic field mapping system constructed	Dec. 2012
1.	**Magnetic field of spectrometer mapped**	**Mar. 2013**
2.a	Detector test chamber available	March 2011
2.b	Electrode surface material selected	June 2011
2.c	First detectors characterized at proton source	Sep. 2012
2.d	DAQ electronics and Trigger working	Sep. 2012
2.e	Data storage and slow control ready	March 2013

Continued on next page

Table 7: Nab project milestones — continued from previous page

	Milestone	Completion
2.f	UHV in spectrometer demonstrated	March 2013
2.g	Electrode system ready	March 2013
2.	**Main detectors work in spectrometer**	**June 2013**
3.a	Shielding calculation for Nab accepted	June 2012
3.b	Neutron guide design finished	Sep. 2012
3.c	Neutron guide ready	June 2013
3.d	Shielding and utilities ready	June 2013
3.	**Spectrometer ready for data taking**	**Sep. 2013**
4.	**Data taken**	**Sep. 2014**
5.	**Data analysis finished**	**Sep. 2015**

Tables 6 and 7 show the significant milestones of the magnet and the Nab projects, respectively. The principal milestones, the ones that lie on the critical path, are shown in boldface. All milestones above the principal ones have to be reached in order to declare the principal milestone achieved. A more detailed schedule is shown in a separate spreadsheet.

9. Summary

We have designed an asymmetric spectrometer optimized for the precise measurements of a, the electron–neutrino correlation parameter, and b the Fierz interferene term, in neutron decay, at the FnPB/SNS.

The device as designed is capable of reaching the physics goals of $\sim 10^{-3}$ relative precision in a and $\sim 3 \times 10^{-3}$ absolute accuracy in b.

We have laid out a realistic breakdown of systematic uncertainties, and a description of the planned procedure for data analysis, fully consistent with the goals of the project.

The asymmetric spectrometer design is realizable in practice, as confirmed by more than one supplier.

We have produced a basic budget for the project based on manufacturer's quotes. We have developed a realistic timeline of the project which starts in 2010, with end of data taking in mid-2014. The critical milestones in this timeline include receiving funding for the spectrometer magnet (mid-2010 in the current plan), taking delivery of the spectrometer (18 months later, start of 2012), detector system and beamline readiness for move-in (start of 2013), and start of data taking (mid-2014).

Finally, we have examined and found feasible in principle the use of the same asymmetric spectrometer for polarized neutron decay experiments, i.e., the electron and proton asymmetry measurements.

References

1. Review of Particle Physics, Phys. Lett. B **667**, 1 (2008), and revisions online at `http://pdg.lbl.gov/2009/`.
2. J.C. Hardy and I.S. Towner, Phys. Rev. C **71**, 055501 (2005).
3. F.J. Gilman, K. Kleinknecht and B. Renk, in *"Review of Particle Physics"*, K. Hagiwara et al., Phys. Rev. D **66**, 01001-113 (2002).
4. A. Sher et al. (BNL 865 Collaboration), Phys. Rev. Lett. **91**, 261802 (2003).
5. T. Alexopoulos et al. (KTeV Collaboration), Phys. Rev. Lett. **93**, 181802 (2004).
6. A. Lai et al. (CERN NA48 Collaboration), Phys. Lett. B **602**, 41 (2004).
7. A. Czarnecki, W.J. Marciano, and A. Sirlin, Phys. Rev. D **70**, 093006 (2004).
8. J. Hardy, I. Towner, Phys. Rev. C **79**, 055502 (2009).
9. G.A. Miller and A. Schwenk, Phys. Rev. C **78**, 035501 (2008).
10. G.A. Miller and A. Schwenk, arXiv 0910.2790 (2009).
11. N. Auerbach, Phys. Rev. C **79**, 035502 (2009).
12. H. Liang, N. Van Giai, and J. Meng, Phys. Rev. C **79**, 064316 (2009).
13. R.W. Pattie, Jr. et al., Phys. Rev. Lett. **102**, 012301 (2009).
14. H. Abele, private communication (2009).
15. H. Abele et al., Phys. Rev. Lett. **88**, 211801 (2002).
16. P. Liaud et al., Nucl. Phys. A **612**, 53 (1997).
17. B. Yerozolimsky et al., Phys. Lett. B **412**, 240 (1997).
18. P. Bopp et al., Phys. Rev. Lett. **56**, 919 (1986).
19. O. Naviliat-Čunčić and N. Severijns, Phys. Rev. Lett. **102**, 142302 (2009).
20. F. Glück et al., Nucl. Phys. A **593**, 125 (1995).
21. T.D. Lee, C.N. Yang, Phys. Rev. **104**, 254 (1956).
22. J.D. Jackson, S.B. Treiman, H.W. Wyld, Phys. Rev. **106**, 517 (1957).
23. N. Severijns, M. Beck, O. Naviliat-Čunčić, Rev. Mod. Phys. **78**, 991 (2006).
24. A. Serebrov et al., Phys. Lett. B **605**, 72 (2005).
25. C.A. Gagliardi, R.E. Tribble, and N.J. Williams, Phys. Rev. D **72**, 073002 (2005).
26. S. Profumo, M.J. Ramsey-Musolf and S. Tulin, Phys. Rev. D **75**, 075017 (2007).
27. V. Cirigliano, private communication (2009).
28. M. Bychkov, et al., Phys. Rev. Lett. **103**, 051802 (2009).
29. P. Herczeg, private communication (2004).
30. `http://pibeta.phys.virginia.edu/`.
31. `http://pen.phys.virginia.edu/`.

32. http://pienu.triumf.ca/.

33. R. Alarcon et al., Nab-Proposal, 2007, http://nab.phys.virginia.edu/nab_proposal.pdf.

34. D. Počanić et al., Nucl. Inst. Meth. A **611**, 211 (2009).

35. P. Huffman et al., Beamline Performance Simulations for the FnPB, private communication, 2005. Initial measurements performed in the FnPB up to the time of this writing are in excellent agreement with the simulation.

36. J. Byrne et al., J. Phys. G: Nucl. Part. Phys. **28**, 1325 (2002).

37. G. Konrad et al., Proceedings of the European COMSOL conference, Grenoble, 2007, http://cds.comsol.com/access/dl/papers/3276/Konrad.pdf.

38. F. Glück et al., Eur. Phys. J. A **23**, 135 (2005).

39. B. Hubbard-Nelson et al., Nucl. Inst. Meth. A **422**, 411 (1999) and http://www.xia.com.

40. R.Grzywacz et al., Nucl. Inst. Meth. B **204**, 649 (2003).

41. D. Dubbers et al., Nucl. Inst. Meth. **596**, 238 (2008).

42. CRC Handbook of Chemistry and Physics, Section 12.

43. S. Baeßler et al., Eur. Phys. J. A **38**, 17 (2008).

44. R. Dobrozemsky, Nucl. Inst. Meth. **118**, 1 (1974).

45. N. A. Robertson et al., Class. Quant. Grav. **23**, 2665 (2006).

46. D. Dubbers et al., arXiv:0812.0347.

47. S.G. Tagare, Phys. Rev. A **34** 1587 (1986).

48. M. Simson et al., Nucl. Inst. Meth. A**611**, 203 (2009).

49. M.A. Lone et al., Nucl. Inst. Meth **174**, 521 (1980).

50. J.S. Nico et al., Phys. Rev. C **71**, 055502 (2005).

51. F. Glück, Phys. Lett. B **436**, 25 (1998).

52. R. Alarcon et al., abBA-Proposal, 2007, http://nab.phys.virginia.edu/ABBA_proposal_2007.pdf.

A. Spectrometer response function parametrization (Method A)

Early in the approval process, the FnPB Program Review and Advisory Committee requested that the Nab, abBA, and PANDA collaborations investigate the feasibility of a common magnetic spectrometer. During the course of the discussions, we concluded that:

1. The main consideration for a successful Nab experiment was the requirement that the time response function should be narrow, in order that the spectrometer characteristics may be determined from the proton TOF edges.

2. The main consideration for a successful abBA experiment was an accurate knowledge of the average of $\cos\theta_0$ for the accepted events, where θ_0 denotes the angle between the electron initial momentum and the neutron spin (or magnetic field in the decay region).

In early 2009, we realized that an asymmetric spectrometer design has significant advantages for Nab:

(i) The upper flight path can be made longer than the lower flight path leading to a narrow time response function.

(ii) By limiting the acceptance of $\cos\theta_0$ to forward-going events, the width of the time-response function could be further decreased.

(iii) Although limiting the range of $\cos\theta_0$ decreases the rate, event rates of several hundred per second are feasible, leading to acceptable run times while maintaining narrow, 2–4%, time response functions.

(iv) The same spectrometer that is optimized for Nab can also carry out measurements of the beta and proton asymmetries in polarized neutron decay.

In this section, we examine the data analysis algorithms and issues of systematic uncertainty for Nab. We go on to show that if the Nab asymmetric spectrometer is used for abBA, the systematic uncertainties in the polarization correlations are smaller than for the original symmetric spectrometer design.

The Nab experiment determines a by measuring the proton yield as a function of proton energy for fixed electron energy. The phase space is shown in Fig. 6.

The Nab spectrometer accelerates protons by 30 keV in order to make possible their detection in a Si detector array. In the adiabatic approximation, the time of flight is given by Eq. (15). We first consider a TOF spectrometer with a magnetic field but no electric field. Time of flight $t_{\rm p}$ has the form

$$t_{\rm p} = \frac{m_{\rm p} L}{p_{\rm p}} f(\cos\theta_0) \equiv t_{\rm min} f(\cos\theta_0)\,, \quad \text{where} \quad f(1) = 1\,. \tag{24}$$

Given a value of $t_{\rm p}$, one can evaluate $p_{\rm p} = (m_{\rm p}L)/t_{\rm p}$. The distribution of $p_{\rm p}$ is obtained by considering the unobserved quantity, $\cos\theta_0$, to be a random variable uniformly distributed between $\cos\theta_{\rm min}$ and 1. A typical magnetic field profile is shown in Fig. 18.

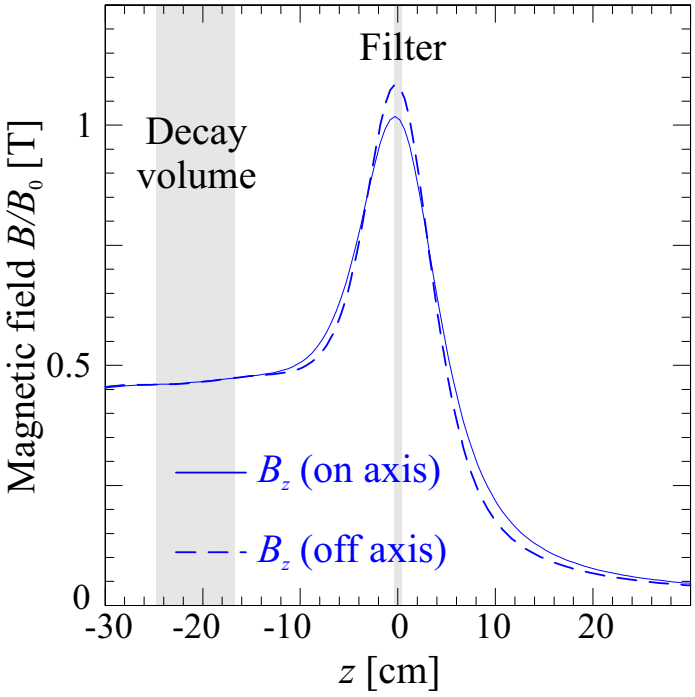

Figure 18: Typical field profile for the decay and filter regions of the spectrometer. The positions of the neutron beam and $\cos\theta$ filter are marked. The ratio of the maximum field to the decay field is 2, and neutrons forward of 45° are transmitted through the field maximum, i.e., $\cos\theta_{\rm min} = 1/\sqrt{2}$.

There is one adjustable parameter in the relationship between momentum and time of flight—the spectrometer length L—which can be determined by plotting the yield against proton energy. Adjusting L should cause all edges to fall into place. (Below we list effects, which cause small deviations.) On the other hand, $Q(t_{\rm p})$, the distribution of $t_{\rm p}$, is given by

$$Q(t_p) = \frac{1}{1-\cos\theta_{\rm min}} \cdot \frac{t_{\rm min}}{|df/d\cos\theta_0|} \,. \tag{25}$$

The width of the distribution for each value of $p_{\rm p}$ is proportional to the minimum time of flight, $t_{\rm min}$. The form of the distribution is independent of $p_{\rm p}$.

What happens when the electric potential is turned on? At first glance, the situation would seem to be complicated. Figure 19 shows the full profile of the electrostatic potential, along with the magnetic field, for the entire length of the spectrometer. The relationship between $t_{\rm min}$ and $p_{\rm p}$ can be calculated from Eq. (15), and from assumed or measured spectrometer geometry and electric potential, or by fitting the relationship between measured locations of TOF edges for $p_{\rm p}$ determined from electron energy $E_{\rm e}$ (see Fig. 6). By applying the $p_{\rm p}$-$t_{\rm p}$ relationship that is determined by fitting the TOF edges to the $t_{\rm p}$ variable, we can bring all the edges into alignment. As an example of the procedure, we consider a spectrometer with a 5 meter flight path. The ratio of the drift field to the decay field is 0.02. The detectors are located in a 50 cm long $B = 1\,$T field. The 30 kV electric potential changes close to the upper detector.

Figure 20 shows how the $t_{\rm min}$ dependence of the product $t_{\rm min} \cdot p_{\rm p}$ changes as the configuration of the spectrometer is modified in several different ways: (a) decay volume is shifted by 20 cm, (b) an electric potential bump of 20 V and 20 cm length is introducted in the TOF region, (c) the electric field is increased by 50%, (d) the accelerating field is shifted, and (e) magnetic field strength is varied.

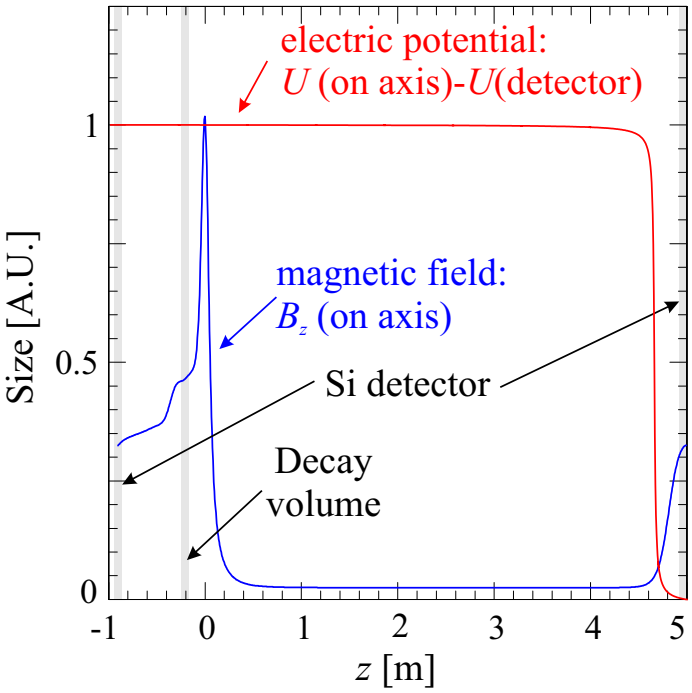

Figure 19: Spectrometer fields. See Fig. 18 for a better view of fields in the decay and filter regions.

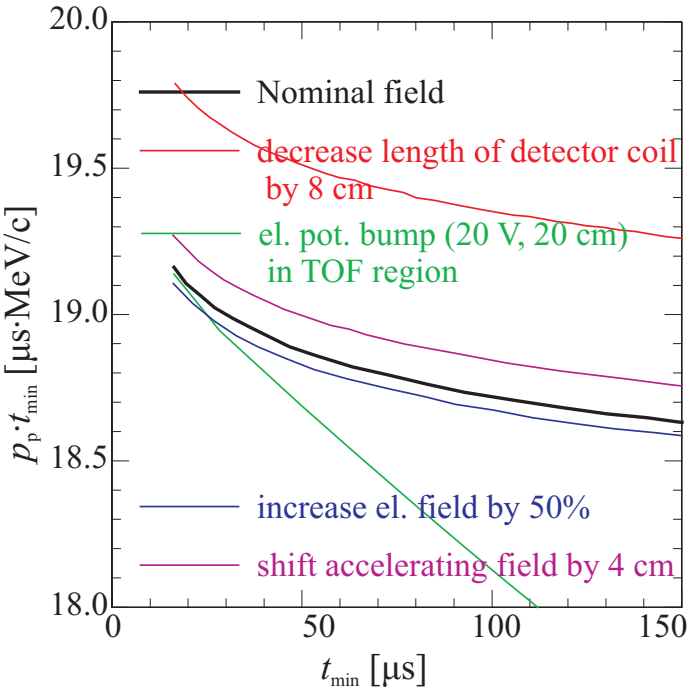

Figure 20: Dependence of $p_{\rm p}t_{\rm min}$ for different spectrometer configurations denoted by different colors in the plot. We note that, if only the magnetic field is changed, $t_{\rm min}$ does not change because the magnetic term in Eq. (15) vanishes for $\cos\theta_0 = 1$, the condition for $t_{\rm p}$ to be minimum.

One can construct the plot of $p_{\rm p}t_{\rm min}$ against $t_{\rm min}$ from the experimental data and then fit the function. We find that the Taylor expansion

$$\ln(p_{\rm p}t_{\rm min}) = \sum_{k=0}^{4} d_k \left(\ln t_{\rm min}\right)^k \tag{26}$$

provides an excellent description of the functional dependence, such that the RMS deviation between the numerical data and the fit is a few times 10^{-7}. With $p_{\rm p}t_{\rm min}$ known, we construct

an estimator for the proton momentum:

$$p_{\rm pe}(t_{\rm p}) = \exp\left[\sum_{k=0}^{4} d_k \left(\ln t_{\rm min}\right)^k\right] . \tag{27}$$

The transformation will align the proton edges in the data with the electron-proton phase space shown in Fig. 6. If no electric field is present, one parameter is required. Five parameters are required with an electric field present. In the next section we discuss what happens away from the edges.

The probability density $Q(t_{\rm p})$ for a given value of $p_{\rm p}$, can be constructed by treating the unobserved quantity $\cos\theta_0$ as a random variable uniformly distributed in the range $\cos\theta_{\rm min} \le \cos\theta_0 \le 1$. Figure 21 presents the typical shapes of $Q(t_{\rm p})$, obtained in realistic GEANT4 simulations.

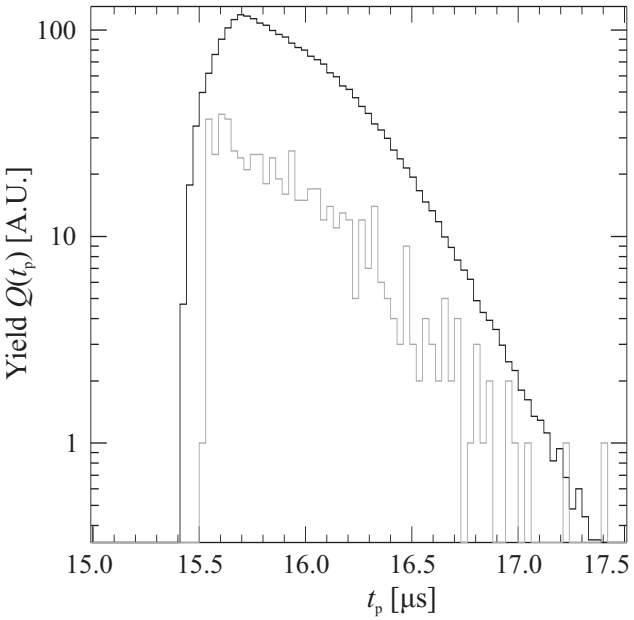

Figure 21: Black curve: typical distribution of proton arrival times in μs for $p_{\rm p} \simeq 0.95\,{\rm MeV/c}$. The exponential tail on the right comes from protons with $\cos\theta_0$ near $\cos\theta_{\rm min}$. These protons take long times to pass over the filter potential. However, there are few such protons. Taken together, the two effects produce an exponential tail. The left edge would be sharp, a step function, for a sufficiently small decay volume. The gray curve shows $Q(t_{\rm p})$ for such a small decay volume. Both curves are results of GEANT4 Monte Carlo simulations.

The shape of the yield dependence on proton energy is obtained by integrating the probability density for $p_{\rm pe}^2/p_{\rm p}^2$. Fig. 22 shows plots of the cumulative event yield against p^2/p_0^2 for several spectrometer configurations, obtained in analytical adiabatic calculations.

Although the proton edges are brought into alignment by adjusting $p_{\rm pe}(t_{\rm p})$, the dispersions in the yield vs $p_{\rm pe}^2/p_{\rm p}^2$ are not. The adjustment of $p_{\rm pe}(t_{\rm p})$ does not require knowing the source of the deviations in $p_{\rm pe}(t_{\rm p})$ from the assumed spectrometer configuration. In Fig. 23, we show how the shift in $p_{\rm pe}^2/p_{\rm p}^2$ is correlated with the variance of $p_{\rm pe}^2/p_{\rm p}^2$ for different spectrometer configurations.

We note that all the proton energy edges for all energies are rounded off by the same resolution function. It follows that the parameters of the resolution function can be determined by a global fit to the complete data set. For all spectrometer configurations mentioned above, we found that

$$\Delta t_{\rm p}(\cos\theta_0) = t_{\rm p} - t_{\rm p,min} = \frac{m_{\rm p}}{p_{\rm p}}\left(-\eta \ln\left|\frac{\cos\theta_0 - \cos\theta_{\rm min}}{1-\cos\theta_{\rm min}}\right| + \rho\left(\cos\theta_0 - 1\right)\right) + \text{a few ns}\,. \tag{28}$$

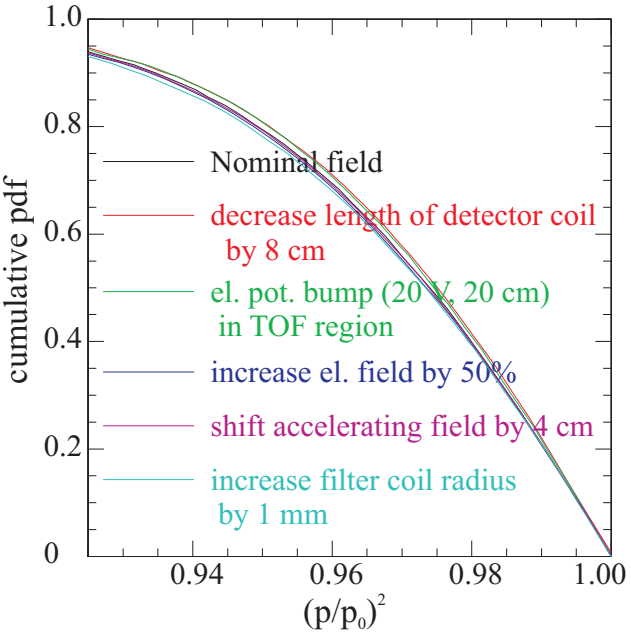

Figure 22: Shape of the proton edges for different spectrometer configurations, calculated analytically. If the proton momentum were longitudinalized in a very short distance or if the spectrometer were very long, the proton edges would be step functions. The non-zero distance over which the proton momentum is longitudinalized rounds off the yield distribution according to Eq. (15).

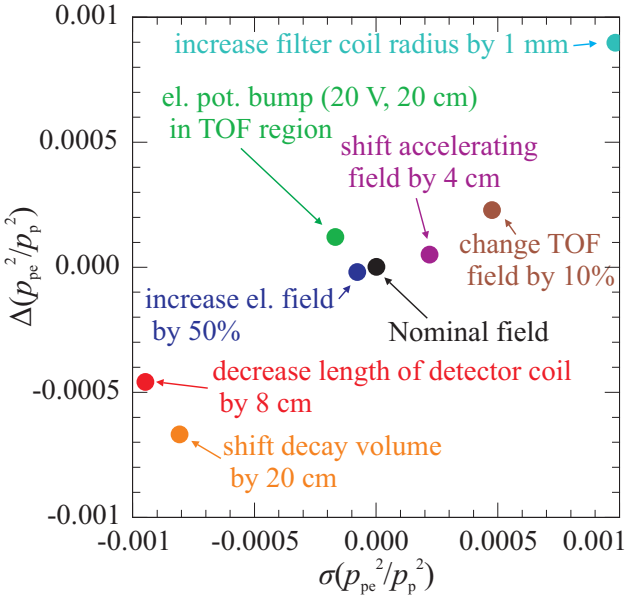

Figure 23: Correlation between the shifts in $\Delta(p_{\rm pe}^2/p_{\rm p}^2)$ and $\sigma(p_{\rm pe}^2/p_{\rm p}^2)$ for different spectrometer configurations. Δ and σ are highly correlated. The fractional changes in these first and second moments when the spectrometer conditions are changed by reasonable amounts are $< 3 \times 10^{-3}$ of the nominal value. The largest change is produced by changing the radius of filter coil by 1 mm in 65 mm. All results shown were obtained in analytical calculations in the adiabatic approximation.

could be calculated from an expression with three free parameters: $t_{\rm p}(\cos\theta_0 = 1)$ (corresponding to the location of the proton energy edge), η (a parameter characteristic of the filter region), and ρ (a length characteristic of the decay and filter regions). The logarithmic singularity at $\cos\theta_0 = \cos\theta_{\rm min}$ arises from the fact that neutrons with just enough forward motion to pass through the filter coil have large values of $t_{\rm p}$. The asymptotic form of the distribution of $t_{\rm p}$ is exponential with a time constant $\tau = \eta m_{\rm p}/p_{\rm p}$. For a current loop with radius r as filter coil, $\eta = \sqrt{2/3}\,r$. We can determine η by measuring the curvature of the field in the filter coil.

If the neutron beam has a nonzero height H, then, to a first approximation, the resolution function $Q(t_{\rm p})$, has its leading edge rounded off by convolution with a uniform distribution

of width H (see Fig. 21). Thus, five parameters are needed to characterize proton energy edges, and three more are needed for the resolution function. These issues require further study and simulation, but at present it appears that we can measure the curvature of the filter field as well as H, and determine ρ in a global fit to the data. We must determine which of these shape parameters entering the function giving the shape of the yield are strongly correlated with a, and measure these parameters. The remaining weakly correlated parameters can be determined in a global fit to the shape of the edges.

B. Statistical uncertainty in Method A

In the original Nab proposal, we showed that if the magnetic and electric fields were perfectly known, a can be determined with a statistical uncertainty $\sigma = 2.3/\sqrt{N}$, where N is the number of events. A total of 6×10^8 events are required to reach the statistical uncertainty of 10^{-4}. Fitting the location of the proton edges and the width of the detection function from the same data set which determines the neutrino electron correlation coefficient a causes an increase in the statistical uncertainty in a. We discuss this for Method A, in which the detection function is described by several fitting parameters. We performed simulated least squares fits to the $1/t_{\rm p}^2$ distributions at 11 electron energies, ranging from 0 keV to 780.78 keV. To have a more general discussion here, we will use a Gaussian detection function:

$$\Phi(1/t_{\rm p}^2, p_{\rm p}^2) \propto \exp\left\{-\frac{(1/t_{\rm p}^2 - E))^2}{2(E\Sigma)^2}\right\}, \tag{29}$$

where the average value for the detection function for a given $p_{\rm p}^2$ is labeled E, and we assume it to be a linear function of $p_{\rm p}^2$, as suggested by Eq. (15). We allow for an offset and denote the two free parameters $E_{\rm low}$ and $E_{\rm high}$, the position of the low and high proton energy edge of the $1/t_{\rm p}^2$ distributions. The relative width of the detection function is denoted by Σ. For $\Sigma = 0$, we rederived

$$a(\Sigma = 0) = \frac{2.3}{\sqrt{N}}, \tag{30}$$

where N is the number of detected events. The increase of the statistical uncertainty is shown in Fig. 24 for a non-zero width of the detection function.

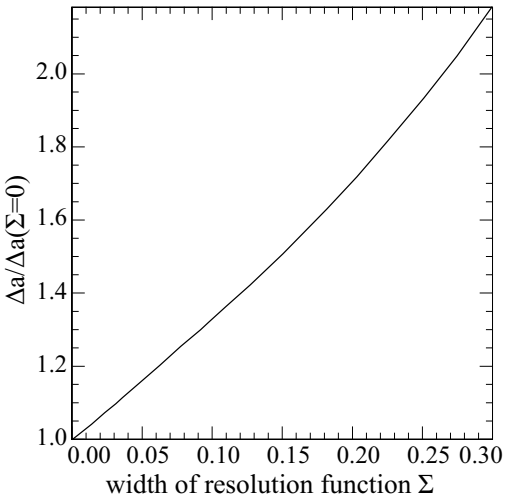

Figure 24: Increase of the statistical uncertainty in a as a function of the relative width of the detection function width Σ. For $\Sigma = 3.8\%$, the increase in the statistical uncertainty in a is 12%.

We conclude that a spectrometer resolution of $\Sigma = 3.8\%$ will not significantly degrade the uncertainty in a from the counting statistics limit. The correlations between a and the other uncertainties are small: $\sigma_{a,E_{\rm low}} \sim 0$, $\sigma_{a,E_{\rm high}} \sim -0.40$, and $\sigma_{a,\Sigma} \sim 0.24$. A task for the near future is to carry out a more general analysis following the model described in App. A, where the five parameters describing the location of the edges and the three parameters describing the shape of the detection function are varied in a global fit. From such a fit we can determine which parameters are strongly correlated with a and must be measured accurately, and which parameters can be determined from the data without increasing the statistical uncertainty in a.

C. Adiabaticity of the proton motion

Some of the discussion in this document relies on results of calculations in the adiabatic approximation. The adiabatic approximation is valid if the relative magnetic field change during one revolution of the proton around the magnetic field line is small. If the adiabatic approximation is valid, we have an adiabatic invariant of motion:

$$\sin^2\theta/B = \text{const.} \tag{31}$$

This adiabatic invariant, together with energy conservation, allows us to use an analytical formula for the proton time of flight $t_{\rm p}$, given in Eq. (15). It is not necessary to work in the adiabatic regime for Nab, but it makes the analysis easier if we do so. A measure of the deviation from adiabaticity is given by an adiabaticity parameter ϵ, defined in Eq. (16). We can test the quality of the adiabatic approximation by reducing the magnetic field by a common factor, which leaves the field shape unchanged. This increases ϵ, but does not alter the proton time of flight $t_{\rm p}^2$ as long as the adiabatic approximation is good (see Eq. (15)). We compared the proton TOF as calculated by GEANT4 (which does not assume adiabaticity) for different values of the magnetic field. In Table 8 we show that at sufficiently high fields we are not sensitive to the size of the magnetic field, as long as we remain in the adiabatic limit. At strongly reduced field strength we become sensitive to the magnetic field reduction. We can verify the results given in this table in our experiment as a means to assess the quality of the GEANT4 simulation (similar to the proposal in Ref. [38]), but this test is complicated to analyze due to the magnetic field dependence of the edge effect.

Table 8: Quality of the adiabatic approximation: the quantities compared, a, proton TOF, and $\overline{\cos\theta_0}$, are insensitive to the field reduction as long as the field is high enough that the adiabatic approximation remains valid. The last row shows the fraction of protons that cannot pass the filter after a field reduction, but could do so at nominal field strength.

Relative B strength:	0.2	0.3	0.5	0.7	2.0
$\Delta 1/t_{\rm p}^2$	-0.4%	-0.1%	-1.6×10^{-4}	-4×10^{-5}	8×10^{-5}
$\Delta a/a$	-4.7%	-1.0%	-0.2%	-0.05%	+0.04%
$\Delta\overline{\cos\theta_0}$	5×10^{-4}	2×10^{-4}	6×10^{-5}	negligible	negligible
Protons lost	0.7%	0.4%	0.15%	6×10^{-4}	5×10^{-4}

This calculation of the effect of nonadiabaticities is preliminary, as we considered only the average TOF change for the different magnetic fields. We neglected the possibility that a proton might be reflected by the filter at a certain field strength, and be able to pass the filter at a different one. This affects only very few protons at or around the nominal field strength. Note that the deviation from adiabaticity, as measured by ϵ, has its dominant effect above the filter.

In conclusion, we can use the adiabatic approximation for the data analysis for both the unpolarized and the polarized experiment.

D. Determination of the solid angle in the polarized experiments

In this Appendix we estimate the error we make when using Eq. (22) for an inhomogeneous field. We denote the number of detected particles in the upper detector for spin-up as $N_{\rm U}^{\uparrow}$:

$$N_{\rm U}^{\uparrow} = \frac{N_0}{2}\int dx\cdot N(x)\cdot \int_{\sqrt{1-r_{\rm B,DV}}}^{1} (1+\alpha\cos\theta_0)\, d\cos\theta_0\,. \tag{32}$$

Here, $N(x)$ is the normalized density of neutron decays, and α is the measured asymmetry, which might be the electron or the proton asymmetry, corrected for the kinematic factors and degree of polarization. Note that now $r_{\rm B,DV}$ depends on the position. We compute

$$\begin{aligned} N_{\rm U}^{\uparrow} &= \frac{N_0}{2}\left[\left(1-\overline{\sqrt{1-r_{\rm B,DV}}}\right)+\frac{\alpha}{2}\overline{(1-1-r_{\rm B,DV})}\right] \\ &= \frac{N_0}{2}\left[\left(1-\overline{\sqrt{1-r_{\rm B,DV}}}\right)+\frac{\alpha}{2}\overline{r_{\rm B,DV}}\right]\,. \end{aligned} \tag{33}$$

The averaging is understood to be performed over the decay volume weighted with the density of neutron decays. Analogously, we get for the count rate in the spin-down state

$$N_{\rm U}^{\downarrow} = \frac{N_0}{2}\left[\left(1-\overline{\sqrt{1-r_{\rm B,DV}}}\right)-\frac{\alpha}{2}\overline{r_{\rm B,DV}}\right]\,. \tag{34}$$

For the asymmetry in the upper detector $\alpha_{\rm U}$, we expect:

$$\alpha_{\rm exp,U} = \frac{N_{\rm U}^{\uparrow}-N_{\rm U}^{\downarrow}}{N_{\rm U}^{\uparrow}+N_{\rm U}^{\downarrow}} = \frac{\alpha\cdot\overline{r_{\rm B,DV}}}{2\left(1-\overline{\sqrt{1-r_{\rm B,DV}}}\right)}\,. \tag{35}$$

For the lower detector, we find

$$N_{\rm D}^{\downarrow} = \frac{N_0}{2}\left[\left(1+\overline{\sqrt{1-r_{\rm B,DV}}}\right)+\frac{\alpha}{2}\overline{r_{\rm B,DV}}\right]\,, \text{and} \tag{36}$$

$$N_{\rm D}^{\uparrow} = \frac{N_0}{2}\left[\left(1+\overline{\sqrt{1-r_{\rm B,DV}}}\right)-\frac{\alpha}{2}\overline{r_{\rm B,DV}}\right]\,. \tag{37}$$

Finally, for the asymmetry $\alpha_{\rm D}$, we get

$$\alpha_{\rm exp,D} = \frac{N_{\rm D}^{\uparrow}-N_{\rm D}^{\downarrow}}{N_{\rm D}^{\uparrow}+N_{\rm D}^{\downarrow}} = -\frac{\alpha\cdot\overline{r_{\rm B,DV}}}{2\left(1+\overline{\sqrt{1-r_{\rm B,DV}}}\right)}\,. \tag{38}$$

These asymmetries have to be subtracted, as shown in Eq. (22), yielding

$$\begin{aligned}\alpha_{\mathrm{exp,U}} - \alpha_{\mathrm{exp,D}} &= \frac{\alpha \cdot \overline{r_{\mathrm{B,DV}}}}{2\left(1 - \overline{\sqrt{1-r_{\mathrm{B,DV}}}}\right)} + \frac{\alpha \cdot \overline{r_{\mathrm{B,DV}}}}{2\left(1 + \overline{\sqrt{1-r_{\mathrm{B,DV}}}}\right)} = \frac{\alpha \cdot \overline{r_{\mathrm{B,DV}}}}{1 - \left(\overline{\sqrt{1-r_{\mathrm{B,DV}}}}\right)^2} \\ &\simeq \frac{\alpha \cdot \overline{r_{\mathrm{B,DV}}}}{1 - \left(\overline{1 - \frac{1}{2}r_{\mathrm{B,DV}} - \frac{1}{8}r_{\mathrm{B,DV}}^2}\right)^2} = \frac{\alpha \cdot \overline{r_{\mathrm{B,DV}}}}{\overline{r_{\mathrm{B,DV}}} + \frac{1}{4}\overline{r_{\mathrm{B,DV}}^2} - \frac{1}{4}\overline{r_{\mathrm{B,DV}}}^2} \\ &= \frac{\alpha}{1 + \frac{1}{4\overline{r_{\mathrm{B,DV}}}}\mathrm{var}\left(r_{\mathrm{B,DV}}\right)}\,. \end{aligned} \tag{39}$$

This equation gives the first correction to Eq. (22) for an inhomogeneous field. For the magnetic field design shown in Fig. 9, the correction is below 10^{-4}, and we can neglect it.

An alternative way to determine the asymmetry would be to measure only α_{U}, and to determine the average emission angle $\overline{\cos\theta_{0\mathrm{U}}}$ through the relative amount of particles which hit the upper detector R_{U} for an unpolarized beam:

$$R_{\mathrm{U}} = \frac{N_{\mathrm{U}}}{N_{\mathrm{U}} + N_{\mathrm{D}}}\,. \tag{40}$$

A direct measurement of R_{U} is probably not very precise, as we have to use count rates of different detectors. We would rather infer it from $R_{\mathrm{D}} = 1 - R_{\mathrm{U}}$ because we can measure R_{D} with protons, where the denominator is measured with the lower detector alone. Protons which are emitted upward are reflected with an electrostatic mirror voltage in the filter region. As our beam is polarized, we have to add count rates with both spin flipper states; the Stern-Gerlach effect and imperfect spin flip efficiency are important corrections. Neglecting these effects, we have

$$R_{\mathrm{U}} = \frac{N_{\mathrm{U}}}{N_{\mathrm{U}} + N_{\mathrm{D}}} = \frac{\frac{N_0}{2}\int dx \cdot N(x) \cdot \int\limits_{\sqrt{1-r_{\mathrm{B,DV}}}}^{1} 1 \cdot d\cos\theta_0}{\frac{N_0}{2}\int dx \cdot N(x) \cdot \int\limits_{-1}^{1} 1 \cdot d\cos\theta_0} = \frac{1 - \overline{\sqrt{1-r_{\mathrm{B,DV}}}}}{2}\,. \tag{41}$$

From R_{U}, we deduce $\overline{\cos\theta_{0,\mathrm{U}}}$ through

$$\overline{\cos\theta_{0,\mathrm{U}}} = \frac{\frac{N_0}{2}\int dx \cdot N(x) \cdot \int\limits_{\sqrt{1-r_{\mathrm{B,DV}}}}^{1} \cos\theta_0 \cdot d\cos\theta_0}{\frac{N_0}{2}\int dx \cdot N(x) \cdot \int\limits_{\sqrt{1-r_{\mathrm{B,DV}}}}^{1} 1 \cdot d\cos\theta_0} = \frac{\frac{1}{2} \cdot \overline{r_{\mathrm{B,DV}}}}{1 - \overline{\sqrt{1-r_{\mathrm{B,DV}}}}}\,. \tag{42}$$

The relative error we make if we just assume $\overline{\cos\theta_{0,\mathrm{U}}} \sim 1 - R_{\mathrm{U}}$ is

$$\begin{aligned}
\frac{1-R_{\mathrm{U}}}{\overline{\cos\theta_{0,\mathrm{U}}}} &= \frac{\left(1-\overline{\sqrt{1-r_{\mathrm{B,DV}}}}\right)\left(1-\frac{1-\overline{\sqrt{1-r_{\mathrm{B,DV}}}}}{2}\right)}{\frac{1}{2}\cdot\overline{r_{\mathrm{B,DV}}}} \\
&= \frac{1-\left(\overline{\sqrt{1-r_{\mathrm{B,DV}}}}\right)^2}{\overline{r_{\mathrm{B,DV}}}} \\
&\simeq 1 + \frac{1}{4\overline{r_{\mathrm{B,DV}}}}\mathrm{var}\left(r_{\mathrm{B,DV}}\right) \ . \qquad (43)
\end{aligned}$$

We note that the first-order correction to any measured asymmetry is small and has the same magnitude as in the previous method. The sign of the correction is different; it is therefore worth to pursue both methods.